

# Kikuchi Pattern Simulations of Backscattered and Transmitted Electrons

Aimo Winkelmann<sup>a,b,\*</sup>, Gert Nolze<sup>c,d</sup>, Grzegorz Cios<sup>a</sup>, Tomasz Tokarski<sup>a</sup>, Piotr Bała<sup>a</sup>, Ben Hourahine<sup>b</sup>, Carol Trager-Cowan<sup>b</sup>

<sup>a</sup>*Academic Centre for Materials and Nanotechnology, AGH University of Science and Technology, al. A. Mickiewicza 30, 30-059 Krakow, Poland*

<sup>b</sup>*Department of Physics, SUPA, University of Strathclyde, Glasgow G4 0NG, United Kingdom*

<sup>c</sup>*Federal Institute for Materials, Research and Testing (BAM), Unter den Eichen 87, 12205 Berlin, Germany*

<sup>d</sup>*TU Bergakademie Freiberg, Institute for Mineralogy, Brennhaugasse 14, 09596 Freiberg, Germany*

---

## Abstract

We discuss a refined simulation approach which treats Kikuchi diffraction patterns in electron backscatter diffraction (EBSD) and transmission Kikuchi diffraction (TKD). The model considers the result of two combined mechanisms: (a) the dynamical diffraction of electrons emitted coherently from point sources in a crystal, and (b) diffraction effects on incoherent diffuse intensity distributions. Using suitable parameter settings, the refined simulation model allows to reproduce various thickness- and energy-dependent features which are observed in experimental Kikuchi diffraction patterns. Excess-deficiency features are treated by the effect of gradients in the incoherent background intensity. Based on the analytical two-beam approximation to dynamical electron diffraction, a phenomenological model of excess-deficiency features is derived, which can be used for pattern matching applications. The model allows to approximate the effect of the incident beam geometry as a correction signal for template patterns which can be reprojected from pre-calculated reference data. As an application, we find that the accuracy of fitted projection center coordinates in EBSD and TKD can be affected by changes in the order of  $10^{-3}$  to  $10^{-2}$  if excess-deficiency features are not considered in the theoretical model underlying a best-fit pattern matching approach. Correspondingly, the absolute accuracy of simulation-based EBSD strain determination will suffer from biases of a similar order of magnitude if excess-deficiency effects are neglected in the simulation model.

Wednesday 28<sup>th</sup> July, 2021 16:29

**Keywords:** Kikuchi diffraction, electron diffraction, EBSD, pattern matching

---

## 1. Introduction

Electron backscatter diffraction (EBSD) [1] is a standard method to obtain spatially resolved crystallographic information via the analysis of Kikuchi diffraction patterns in the scanning electron microscope (SEM).

In the field of EBSD data analysis, pattern matching approaches using quantitative Kikuchi diffraction simulations [2–6] are increasingly applied in investigations of the crystallographic properties of materials. This concerns, for example, the discrimination of pseudosymmetric pattern variants, which can be difficult to detect by conventional EBSD system software. Investigations of this type include the effects of polarity [7, 8], chirality [9–12], or the correct orientation of tetragonal or other low-symmetry structure variants [13–15]. Phase differentiation is discussed in [16]. Kikuchi diffraction simulations are also applied to estimate continuous parameters from experimental patterns. This includes the calibration of the geometrical setup

---

\*corresponding author

Email address: [winkelmann@agh.edu.pl](mailto:winkelmann@agh.edu.pl) (Aimo Winkelmann)

[17–20], the indexing and refinement of crystal orientations [8, 21–27], and the quantification of local changes in lattice parameters [28–31], including the possible role of defects [32].

In order to improve the simulation-based pattern matching approaches, it is necessary to understand which experimental effects are relevant to be included in the theoretical models used in Kikuchi diffraction pattern simulations. In this way, also the possible intrinsic accuracy and precision of simulations for pattern matching approaches can be better understood, including the development of new indexing approaches using synthetic test data [33–37].

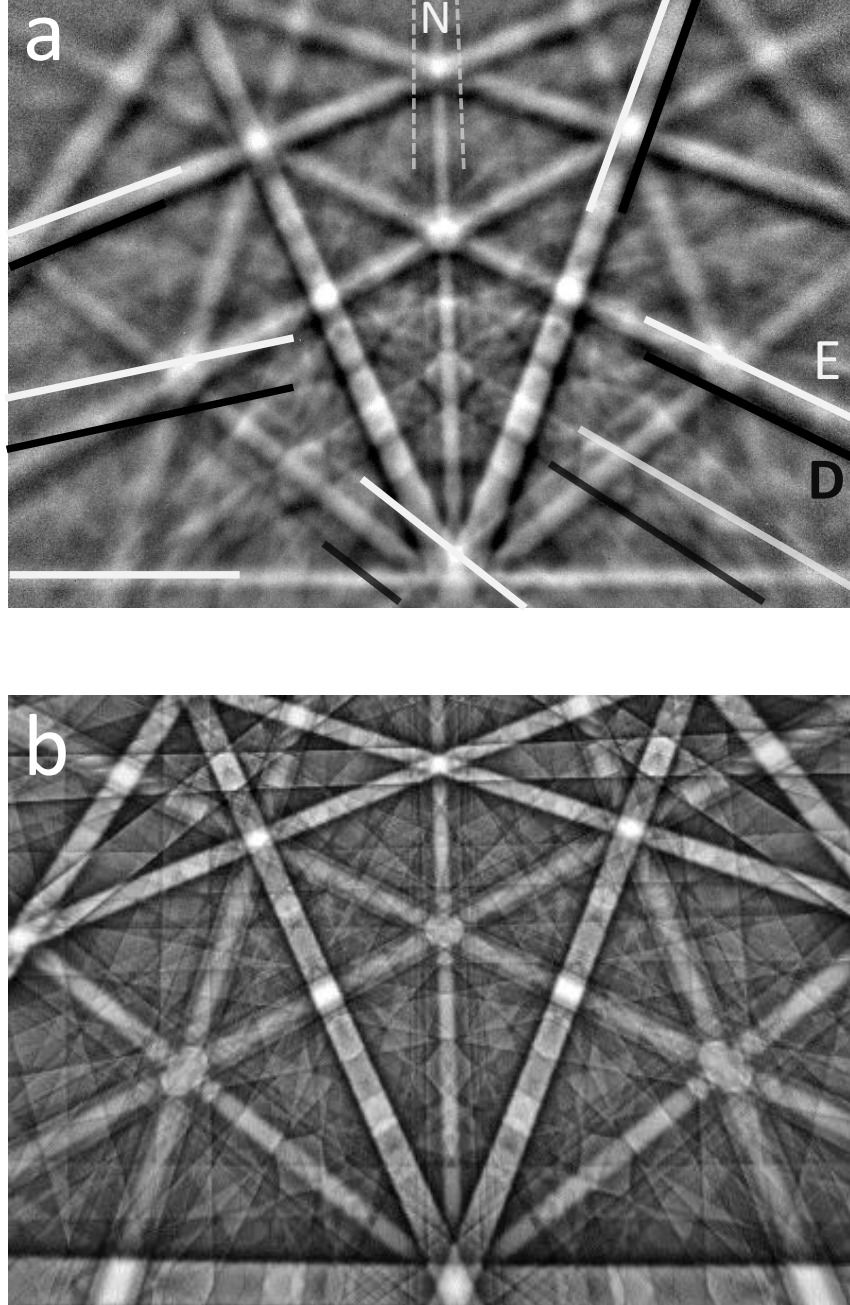


**Figure 1:** (a) Excess-Deficiency effects in a Kikuchi pattern measured from troilite (FeS), at 20kV primary beam acceleration voltage. Pronounced excess (E) and deficiency (D) lines are observed on Kikuchi bands which are inclined relative to the vertical direction in the pattern. Bands which run nearly vertical (N) do not show a significant excess-deficiency asymmetry. (b) Dynamical Kikuchi pattern simulation according to [2]. While the main bands are visible in both patterns, the illumination-like, excess-deficiency effect of the Kikuchi bands in the experiment is not reproduced by the simulation due to the neglect of diffraction effects of the diffusely scattered electrons.

The simulation models which are currently used in EBSD pattern matching studies are mostly based on the Bloch wave approach to dynamical electron diffraction, which can be applied to the problem of channeling effects in localized incoherent electron scattering as demonstrated in [38–41]. For the case of EBSD patterns, the Kikuchi patterns can be well described by diffraction effects from point emitters of backscattered electrons which are localized at atomic positions [3]. Key assumptions concerning the treatment of inelastic scattering and the resulting electron energy spectrum relevant for the Bloch wave simulations [42] have been confirmed by the analysis of plasmon and phonon scattering in a multislice treatment of EBSD Kikuchi patterns [43, 44]. The interpretation of Bloch wave solutions in terms of quantum trajectories [45, 46] can potentially provide a framework for the consistent combination of classical Monte Carlo trajectory simulations with the interference effects of electron diffraction. Because multislice treatments of EBSD Kikuchi patterns [47, 44] are not limited to perfect crystals, they can also be a powerful tool to study the specific influence of defects in the observed diffraction patterns.

Most of the Kikuchi diffraction simulations discussed above involve an approximation which neglects some specific diffraction effects related to the direction of the incident beam. In this approximation, a single global reference dataset can be used to reproject pattern templates for any given geometrical setup and orientation, which avoids a time-consuming dynamical re-simulation which otherwise would be necessary for each different crystal orientation relative to the incident beam.

Incident-beam related effects include the characteristic features of excess and deficit lines, which are also well known from Kikuchi patterns in transmission electron microscopy (TEM) [48–57]. As an example of excess-deficiency (E/D) effects in an EBSD pattern, we show in Figure 1a a Kikuchi pattern measured from a troilite (FeS) grain in a meteorite sample. A number of Kikuchi bands appear like they are illuminated from the top, with the Kikuchi band edges showing an excess line "E" combined with a deficit line "D". For comparison, we show in Figure 1b a Kikuchi pattern simulation which neglects the diffraction of the diffusely scattered electrons, i.e. this corresponds to the approximation which is used in essentially all the pattern matching studies mentioned above. The simulation shown in Figure 1b shows an overall good agreement with the main experimental Kikuchi bands, but the illumination-like, excess-deficiency effect of the Kikuchi bands in the experiment is not reproduced by the simulation. As we will discuss in this paper, the excess-deficiency effects can be described by a diffraction model which considers the effect of an intensity gradient in the angular distribution of the incoherent diffuse background electrons. The model will also explain why those Kikuchi bands which run nearly vertical in Figure 1a (N) do not show a significant excess-deficiency asymmetry.

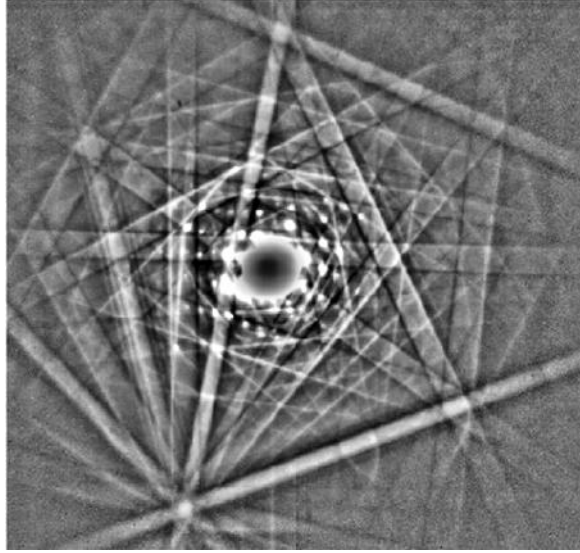
Excess-deficiency effects are also relevant in the special technique of transmission Kikuchi diffraction (TKD) [58–69]. In Figure 2, we show examples for different Kikuchi diffraction features which have been observed in transmission measurements in the SEM and TEM. The pattern of Figure 2a from a 200 nm thick Mg sample was studied at 30 kV in [66]. This sample is thin enough for a discrete spot pattern to be observed in the center of the pattern. In the outer region of the pattern, Kikuchi bands are observed with a central band intensity that is higher than the average background, and which show E/D effects with the higher intensity band edge towards larger distances from the direct beam spot pattern. These bands are created after "absorption" due to large-angle phonon scattering from the direct beam. Note that the pattern of Figure 2a is overexposed in the central area and further processed to cover the large dynamic range between the very high-intensity diffraction spots and the low intensity background Kikuchi pattern. For comparison, Figure 2b shows increased absorption in a 1500 nm thick sample from a 100 kV TEM study in [70], with Kikuchi bands of lower intensity than the average background. Diffraction spots are absent in Figure 2b, but the diffusely broadened incident beam in the center of the pattern still has a relatively high intensity compared to the outer regions of Figure 2b. The dark bands on this high background correspond

to missing intensity that is "absorbed" from the local intensity by localized, large angle phonon scattering. However, this intensity is not "lost" but it can re-appear at large scattering angles and then result in the light bands of part Figure 2a after additional subsequent diffraction. In the outer regions of Figure 2b, with a strong intensity gradient, the E/D band edges can also be clearly seen. In a situation which is intermediate between Figure 2a and Figure 2b, there would be excess bands observed in the low intensity outer region of Figure 2b, which would change to the dark bands in the central region. Figure 2c shows the limiting case of a 1000 nm thick Si sample studied at 15 kV by TKD in [66], where the dark Kikuchi bands dominate, and E/D are very much reduced due to the more even distribution of intensity by continued beam broadening. For systematic TEM measurements in an energy range between 50 and 1200 kV, see also [50, 51].

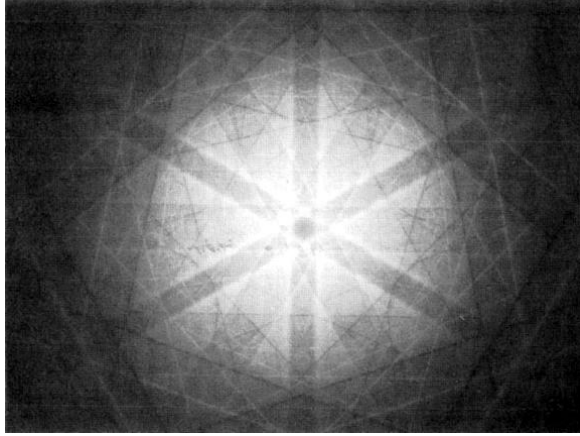
The inclusion of the discussed E/D effects in Kikuchi pattern simulations should allow to better understand the implications of these effects for the precision and accuracy of pattern matching applications. A quantitative comparison of experimental Kikuchi patterns with simulations in which we can switch on or off the E/D effect will show the systematic bias which is introduced, for example, in fitted crystal orientation data and in the projection geometry when using pattern matching approaches. As we will show, a neglect of E/D effects critically limits the level of the realistically possible parameter accuracy when matching actual experimental Kikuchi patterns against simulations.

This paper is structured as follows. We will first recall some basic properties of diffuse scattering in the context of EBSD Kikuchi patterns, and then discuss the Thomas-Humphreys many-beam model [55, 71] of diffuse Kikuchi diffraction. For real-time simulations, we derive a phenomenological model based on the two-beam approximation to include E/D effects in pattern matching applications via a correction of the conventional pattern templates. The simplified analytical model combined with image processing techniques can efficiently emulate the phenomenological effects in experimental Kikuchi patterns, which we show by a quantitatively significant improvement of the image similarity between experiment and simulation. In comparison to the existing theoretical studies which have revealed the fundamental Kikuchi diffraction mechanisms [49, 55, 71, 38, 72], the present paper does not contain any fundamentally new theoretical developments, but instead we aim at a consistent treatment of the resulting experimental phenomena for pattern matching applications in EBSD and TKD.

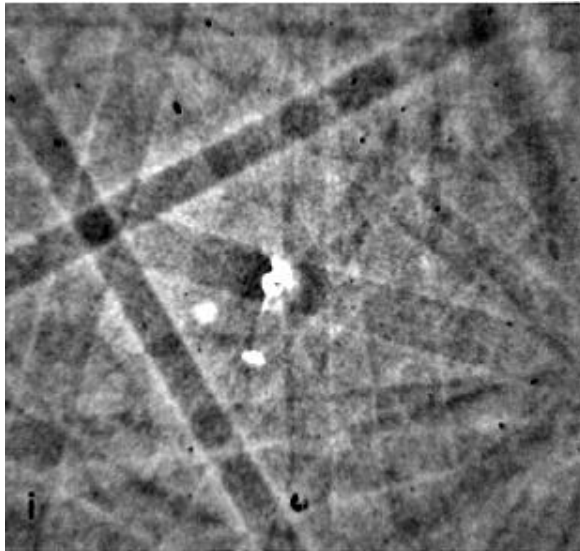
As an application of the refined simulation model, we use the example of projection center determination from an experimental Kikuchi patterns measured by conventional EBSD in a backscattering geometry, as well as by transmission Kikuchi diffraction. We demonstrate that systematic errors in the order of at least 1% in the relative position of the projection center can be introduced by not including E/D effects in the simulations, which has corresponding effects for a quantitative determination of lattice parameters and strain states via simulated Kikuchi patterns. Several existing estimations of the absolute precision of pattern matching approaches for projection center and strain determination have been based on analyses of simulated synthetic data without E/D effects [19, 30, 73], which thus potentially introduces a corresponding bias. Finally, we will show that the refined simulation model is able to reproduce contrast formation under various different conditions which are relevant for both SEM as well as TEM Kikuchi diffraction patterns.



(a) Mg,  $V_0=30\text{kV}$ ,  $d=200\text{nm}$ .



(b) Si,  $V_0=100\text{kV}$ ,  $d=1500\text{nm}$ .



(c) Si,  $V_0=15\text{kV}$ ,  $d=1000\text{nm}$ .

**Figure 2:** Kikuchi patterns which were observed in transmission measurements, illustrating the combined role of acceleration voltage ( $V_0$ ) and sample thickness ( $d$ ) in the contrast formation of Kikuchi bands. Data in (a) and (c) reproduced from Fig.7 and Fig.3i in Brodu *et al.* [66]; data in (b) reproduced from Figure 5c in Reimer [70].

## 2. Theoretical Background

### 2.1. Diffuse Electron Scattering and Kikuchi Diffraction

The general treatment of diffuse electron scattering in connection with diffraction effects is of considerable complexity because different types of inelastic processes and various coherent and incoherent contributions need to be treated simultaneously to determine the final scattered intensity from a crystal, including the possible effects on subsequent microscopic imaging. Overviews about the relevant effects and the extensive literature on the subject can be found in [74–78].

In the following, we will use the term ”diffuse scattering” to refer loosely to scattering processes which lead to a beam broadening and redistribution of intensity, which is not related to coherent scattering relative to an external incident beam of electrons. Diffuse scattering in the sample introduces uncontrolled phase shifts into the scattering pathways and thus lifts the restrictions of only discrete momentum transfers to the incident beam by the lattice. This relaxation of interference conditions will cause (a) an intensity reduction of the coherent diffraction spots and (b) the simultaneous appearance of intensity between the diffraction spots. Similarly, the coherent features of diffraction disks in convergent beam electron diffraction (CBED) and related techniques using externally shaped beams will be affected by diffuse scattering.

Kikuchi Diffraction can be considered as a special case of diffuse scattering, in which inelastic scattering leads to the formation of secondary divergent sources of electrons inside the sample. Kikuchi patterns are formed due to the subsequent diffraction of these inelastically scattered electrons by the crystal structure. In the theoretical models of Kikuchi diffraction, the possible coherence between electron waves on various scattering pathways before and after the inelastic scattering events needs to be considered. Because the underlying crystal geometry of Bragg reflections is the same for coherent and incoherent scattering, the resulting overall diffraction profiles are combined of different, superimposed shapes [49, 79–81, 38, 72, 82–85, 39, 86]. Quantitative experimental measurements of diffuse scattering can be challenging, because, for example, there can be differences of several orders of magnitude between the intensities of coherent diffraction spots and the low-intensity diffuse intensity features.

Experimental Kikuchi pattern features in TEM and SEM share many similarities, which are discussed, for example, in [70, 87–89]. Compared to the situation in a TEM, however, the conventional EBSD setups usually involve very large scattering angles ( $\approx 40\text{--}130^\circ$ ), relative to the primary beam of the SEM as well as to the sample surface. Due to the reduction of atomic scattering factors with angle and the simultaneous increase of incoherent scattering, the discrete spot diffraction effects of the primary electrons at smaller angles can be excluded from the EBSD measurement most of the time.

The strong influence of the scattering geometry on the resulting diffraction effects can be seen by the differences of conventional reflection-EBSD to the special method of on-axis TKD [66], which involves a transmission geometry very similar to a TEM, and in which spot diffraction patterns can dominate the transmitted intensity for thin samples. Due to the transmission geometry, thickness-dependent absorption effects influence the contrast of Kikuchi bands in on-axis and off-axis TKD more than in the typical backscattering geometry of conventional EBSD [90, 63, 91, 66, 68].

With respect to simulation models, the specific EBSD scattering geometry in the SEM allows a significant simplification of the theoretical description. In many cases, the Kikuchi features at large scattering angles and low energy losses relative to the incident beam can be described as resulting from atomic emitters of backscattered electrons [85, 39]. In terms of the relevant energy spectrum, the trajectories of the backscattered electrons in the tilted EBSD geometry (sample tilts are often near  $70^\circ$  relative to the primary beam) emphasize the conservation of diffraction contrast only for relatively low energy losses relative to the primary beam energy, while diffraction contrast largely disappears for increasing energy losses [92, 93, 42, 94, 44].

Even in the absence of diffraction features in the outgoing electron distribution, however, incident beam diffraction effects can still influence the transport effects of inelastic electrons and the intensity distribution of the diffuse background in EBSD Kikuchi patterns, as can be shown, for example, by measurements of backscattered Kikuchi patterns for different positions in an incident beam channeling pattern [95]. These incoherent background effects are usually removed by image processing from the raw Kikuchi signal (e.g. by high pass filtering). However, as we will discuss in the next section, there will be surviving diffraction effects even of an incoherent outgoing intensity, which result from the *gradients* of intensity in the diffuse background as well as from anomalous absorption effects inside a crystal.

## 2.2. Mechanisms of Kikuchi Pattern Formation in EBSD and TKD

In this section, we provide a qualitative discussion of the key mechanisms which will motivate the subsequent derivation of specific numerical simulation models, which will then be presented in sections 3.1 and 3.2 below.

In Figure 3, we give a schematic overview of the interplay between various scattering processes which are relevant in experimental Kikuchi diffraction measurements. Kikuchi diffraction involves a two-step mechanism, which starts with inelastic incoherent electron scattering that is followed by coherent re-scattering (diffraction) in a crystal [96]. In Figure 3, the basic two-step nature is illustrated by the schematic separation of an effectively divergent electron source in the upper part of the figure, which is followed by coherent elastic scattering in a diffracting crystalline region in the lower part of the figure.

For the purposes of the theoretical framework of realistic simulations, we argue that Kikuchi diffraction pattern formation is dominated by the interplay of the following mechanisms, which will be discussed subsequently:

- the three-dimensional geometry of Bragg reflections
- the relative coherence of different electron waves after various scattering processes
- the dynamical diffraction of electrons from coherent point emitters
- the dynamical diffraction of an incoherent diffuse intensity distribution
- excess-deficiency effects due to background intensity gradients within the range of Bragg angles of Kikuchi bands
- anomalous absorption due to the different localization of inelastic scattering processes in a crystal

### 2.2.1. Geometry

Relative to a divergent source of electrons, Bragg's law is traced out by Kossel-cones [89], which describe all three-dimensional directions with a constant Bragg angle  $\theta_{\text{Bragg}}$  relative to a given lattice plane. For each reciprocal lattice vector  $\vec{g}$ , there is a corresponding Kossel cone described by those wave vectors  $\vec{K}$  which have a component of  $|\vec{g}|/2$  along the direction of  $\vec{g}$ :

$$\vec{K} \cdot \frac{\vec{g}}{|\vec{g}|} = \frac{|\vec{g}|}{2} \quad (1)$$

Equivalent Kossel cones are fixed to  $\vec{g}$  and  $-\vec{g}$ , resulting in a geometrical width of  $2\theta_{\text{Bragg}}$  of a Kikuchi band. The geometrical positions of Bragg reflection are also called Bragg lines, in order to emphasize their geometrical meaning, which plays a general role in various diffraction effects of internal as well as external sources [97, 98].

The Kossel-cone construction of Eqn. 1 describes only the underlying geometry of possible Bragg reflections near the edges of Kikuchi bands. Geometrical Kossel cones are independent

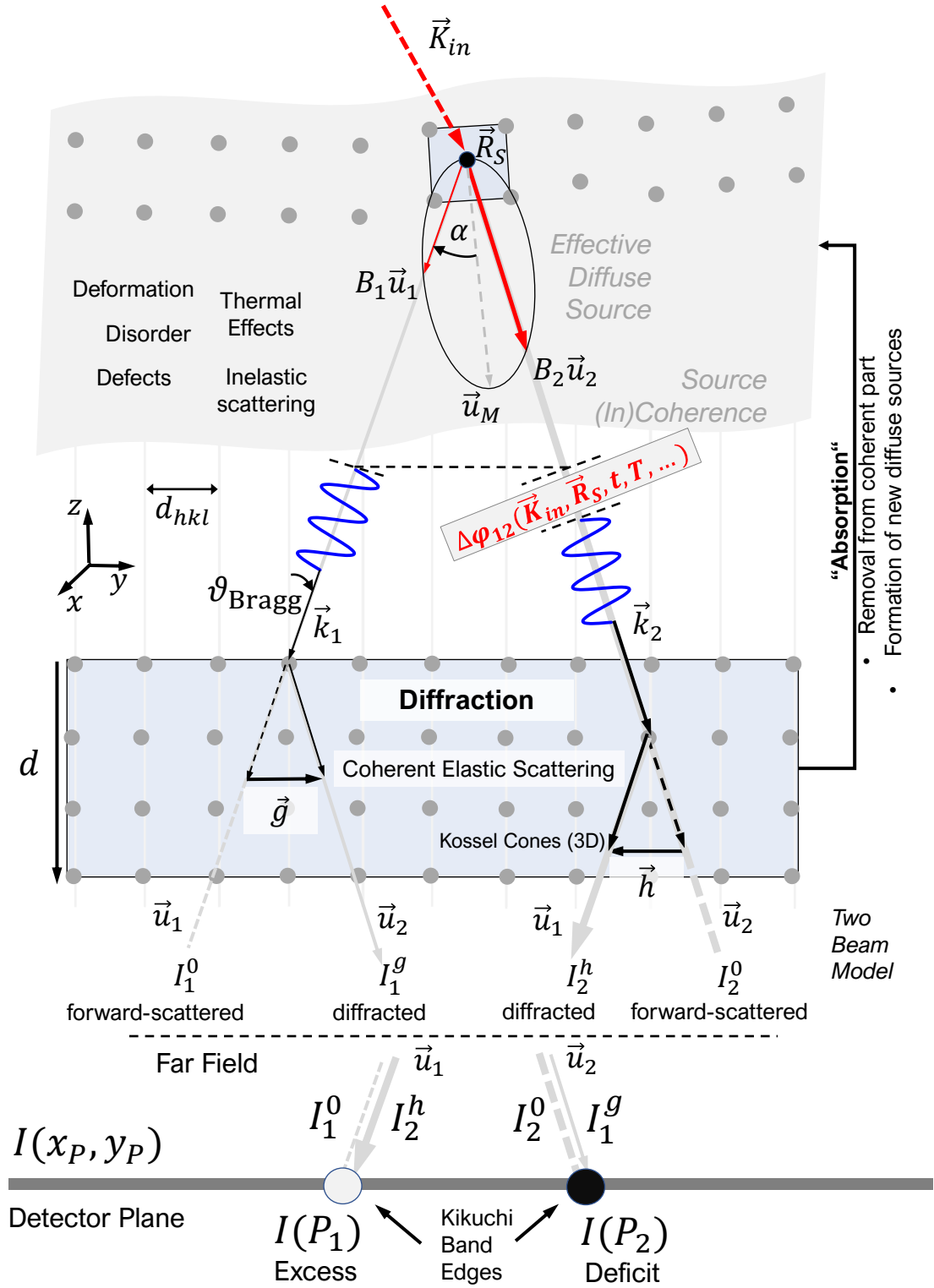


**Figure 3:** Model for the formation of excess-deficiency features in Kikuchi diffraction patterns via coherent scattering of intensity from a divergent incoherent source of electrons. For details see the main text.



of the actual position of the divergent electron source inside the crystal unit cell, and thus the actual intensity distribution in a Kikuchi pattern cannot be explained by Bragg's law in Eqn. 1 alone. Instead, the observed contrast, and the measured width of experimental Kikuchi features is determined by dynamical electron scattering effects in connection with the specific localization of the divergent source relative to the periodically arranged surrounding atoms, and to the coherence between electron waves emitted along different directions  $\vec{u}$ .

### 2.2.2. Scattering Processes and the Role of Coherence

In Figure 3, the interplay of various scattering effects in Kikuchi diffraction is illustrated schematically. The model considers dynamical diffraction after single diffuse scattering events [38], while incident beam diffraction effects are neglected. We assume a divergent source of electrons which is located at  $\vec{R}_S$ . An incident beam with wave vector  $\vec{K}_{in}$  is inelastically scattered, forming a source of diffuse intensity [99]. Diffusely scattered electrons will have a changed wave vector and direction, which is shown by two examples  $\vec{k}_1$ , and  $\vec{k}_2$ , respectively, with the probabilities  $B_1$  and  $B_2$  of being scattered into the corresponding directions  $\vec{u}_1$ , and  $\vec{u}_2$ , respectively. The key mechanism of Kikuchi pattern formation is that the wave vectors  $\vec{k}_1$  and  $\vec{k}_2$  can have completely random phases (e.g.  $\Delta\phi_1$  and  $\Delta\phi_2$ ) relative to an incident reference wave  $\vec{K}_{in}$ , while they can maintain controlled phases  $\Delta\phi_{12}$  relative to each other, as determined by their common origin at  $\vec{R}_S$  (in the absence of any further incoherent scattering events after  $\vec{R}_S$ ).

As is indicated in the upper part of Figure 3, the diffuse scattering can be caused, for example, by thermal effects (phonon scattering), inelastic losses due to electronic excitations and core level losses, as well as by deformations, disorder and defects in the crystal [99]. For these processes, the relative phase  $\Delta\phi_{12}$  between waves moving into directions  $\vec{u}_1$  and  $\vec{u}_2$  can be known to different degrees for scattering events of individual electrons, i.e. for each scattered electron, the phase  $\Delta\phi_{12}$  could depend on  $\vec{K}_{in}$ ,  $\vec{R}_S$ , the temperature  $T$ , or the time  $t$ , for example.

We assume two limiting cases:

- (I) A coherent point emitter (CPE) at  $\vec{R}_S$ . The CPE diffraction pattern will depend explicitly on  $\vec{R}_S$  relative to the surrounding atoms. The phases  $\Delta\phi_{12}$  are prescribed by the fixed position of the electron emission event at point source  $\vec{R}_S$  and a fixed phase difference for each electron emission event (for a point source, we can set  $\Delta\phi_{12} = 0$  for all directions  $\vec{u}$ ).
- (II) A completely incoherent diffuse intensity (IDI) distribution. Scattered waves for different directions  $\vec{u}$  have uncontrolled phases. For each different emission event, the relative phase  $\Delta\phi_{12}$  is assumed to fluctuate randomly. The IDI diffraction pattern will *not* depend explicitly on  $\vec{R}_S$ .

The diffraction of  $\vec{k}_1$ , and  $\vec{k}_2$  is completely independent of each other in case (II), whereas there is a known phase relationship in case (I) which leads to additional interference effects between  $\vec{k}_1$ , and  $\vec{k}_2$  for the coherent point emitter. Case (I) also includes a coherent point emitter in a perfect crystal, i.e. the diffracting crystalline region extends to include  $\vec{R}_S$  at an atomic position of the crystal. Case (II), in principle corresponds also to incident electrons from an external incoherent electron source (basically with  $\vec{R}_S$  at infinity) which are dynamically scattered by a crystalline region of thickness  $d$ .

The basic Kikuchi mechanism can be reproduced by a double-scattering cluster model [100]. Such a model shows that the loss of a predictable phase relationship after a first incoherent scattering event leads to the disappearance of the discrete spot pattern, as is usually described by a Debye-Waller factor due to thermal diffuse scattering. However, a Kikuchi-pattern can be formed by the electrons lost from the coherent portion, due to the fixed geometry of the

pathways relative to scattering centers which are fixed at atomic positions. Using the double-scattering cluster model in [100] it can be argued that Kikuchi diffraction pattern formation is stabilized by the fact that thermal movements of atoms, on the one hand, are large enough relative to the wavelength of the incident beam (randomizing the phase of the scattered waves relative to the incident beam), while, on the other hand, these atomic displacements are still small relative to the lattice spacing of the surrounding crystal (providing a relatively fixed source point for subsequent coherent scattering).

The schematic model of Figure 3 neglects incident beam diffraction effects acting on the wave vector  $\vec{K}_{in}$ . In the general case, controlled phase relationships can be introduced by dynamical diffraction of the single vector  $\vec{K}_{in}$  into a set of mutually coherent incident waves, which undergo inelastic scattering at  $\vec{R}_S$  and which are then subsequently diffracted and interfere in the outgoing path. This situation can be described by the mixed dynamic form factor [101, 76, 102]. In this picture, the crystal acts as a beam splitting and beam combination device which allows to measure interference features that are determined by the properties of the specific inelastic scattering processes.

In the following, we will neglect any additional interference due to the incident beam in the model of Figure 3 and discuss the limiting cases of perfect coherence and complete incoherence of waves along two directions  $\vec{k}_1$  and  $\vec{k}_2$  which will result in different Kikuchi features for  $\vec{k}_1$  and  $\vec{k}_2$  travelling near Kossel cones in a crystal.

### 2.2.3. Diffraction from Coherent point emitters (CPE)

If the source emitter positions  $\vec{R}_S$  in Figure 3 are fixed to a perfect crystal at atomic positions, the resulting Kikuchi diffraction pattern can be calculated using the reciprocity principle for a beam incident from the direction  $-\vec{k}_P$  on a detector pixel. The corresponding dynamical diffraction effects can be treated using Bloch wave models of contrast formation due to electron channeling and large-angle scattering in crystals [40, 41]. Applications of this approach to the simulation of electron backscatter diffraction have been presented in [2–5].

For different chemical elements in a crystal, the backscattered intensity is determined by calculating the overlap of the wave function  $\Psi$  with the backscattering atoms at their respective  $\vec{R}_S$  and weighting by the  $Z^2$ -dependence of scattering cross sections in the Rutherford model. Different emitter positions in the unit cell can produce different Kikuchi patterns, which can be shown by measuring the energy loss due to the different recoil energy of different backscattering atoms, see the example of sapphire  $\text{Al}_2\text{O}_3$  demonstrated in [103]. Random positions of the emitters  $\vec{R}_S$  in the unit cell lead to averaging out of the individual, site-dependent Kikuchi patterns [104]. A completely similar treatment is possible for photoelectrons, which are emitted from atomic core levels due to excitation by X-rays [105]. In the following, we call these contributions a coherent point emitter (CPE) Kikuchi pattern, where the coherence refers to the waves emitted in different directions from the same source  $\vec{R}_S$ . The waves from different sources  $\vec{R}_S$  are considered as completely incoherent, as resulting from the recoil energy loss and multi-phonon excitation in the large-angle scattering event [103].

### 2.2.4. Diffraction of Incoherent Diffuse Intensity (IDI)

Incoherent scattering of the waves  $\vec{k}_1$  and  $\vec{k}_2$  is characterized by a randomization of their relative phase. This leads to a loss of the CPE Kikuchi features, which are based on standing wave formation by interference. Incoherent scattering can explain the loss of Kikuchi pattern contrast in connection with plasmon scattering, which is not localized at specific points in the unit cell [93, 94, 44]. The loss of CPE Kikuchi contrast observed after inelastic scattering in energy-resolved experiments can be simulated by a phenomenological reduction of the interference terms in the Bloch wave model [94].

Assuming completely random phases between waves traveling in different directions  $\vec{u}$ , we have an IDI distribution, which is characterized by the direction-dependent intensity factor  $B(\vec{u})$ .

In one limit, if  $B(\vec{u})$  would be constant, the diffraction effects in the crystalline region would scatter intensity symmetrically and no diffraction contrast would be seen.

A different limit is reached when  $B(\vec{u})$  would be very sharply peaked, for example effectively limiting intensity to the direction  $\vec{k}_2$  only. This situation corresponds to an electron source outside of the crystal and diffraction of an incident electron beam  $\vec{k}_2$ , resulting in a spot pattern formed by reflections along the wave vectors  $\vec{k}_2 + \vec{g}$ . Increasing the divergence of the incident electron distribution (for example assuming a constant intensity within a given angular range relative  $\vec{k}_2$ ) would then describe, for example, convergent beam electron diffraction (CBED) [98], and electron Kossel patterns [106] (where the divergence is large enough to cause diffraction disks to overlap).

The discussion so far already points to a way to simulate the diffraction effects of the IDI by considering separately the incoherent waves travelling along different directions  $\vec{u}$  and summing up the diffraction patterns weighted by an angle-dependent weight  $B(\vec{u})$ . This will be explained in Section 3.1.

### 2.2.5. Excess-Deficiency Mechanism

In the general situation of a large-angle gradient in an incoherent diffuse intensity distribution, the complementary scattering by reciprocal lattice vectors  $+\vec{g}$  and  $-\vec{g}$  leads to excess-deficiency lines, because more intensity can be diffracted away by  $+\vec{g}$  from the high intensity region than can be scattered by  $-\vec{g}$  from the low intensity region [97]. Similarly, a gradient in the coherent emission intensity will also cause excess-deficiency effects for the CPE Kikuchi features [57].

The formation of excess-deficiency features at Kikuchi band edges can be explained by considering the separate diffraction of electrons by reciprocal lattice vectors  $\vec{g}$  and  $\vec{h} = -\vec{g}$  in terms of a two-beam model as shown in Figure 3. To indicate the origin of different partial intensity contributions  $I_j^g$ , we use a subscript  $j$  to label the direction before diffraction, and a superscript  $g$  to indicate the reciprocal lattice vector responsible for a reflection. For the two-beam model in Figure 3, the total observed intensity at a point  $P_1$  in direction  $\vec{u}_1$  is

$$I(P_1) = I_1^0 + I_2^h \quad (2)$$

where  $I_1^0$  is the direct intensity remaining in direction  $\vec{u}_1$  after dynamical scattering, while  $I_2^h$  is reflected towards  $\vec{u}_1$  by  $\vec{h}$  from the different initial direction  $\vec{u}_2$ .

Correspondingly, the total observed intensity at a point  $P_2$  in direction  $\vec{u}_2$  is

$$I(P_2) = I_2^0 + I_1^g \quad (3)$$

where  $I_2^0$  is the direct intensity remaining in direction  $\vec{u}_2$ , while the additional intensity  $I_1^g$  comes from the different direction  $\vec{u}_1$  via reflection by  $\vec{g}$ .

For a given crystal thickness, the intensities  $I_1^0$  and  $I_1^g$  include the relative intensity factor  $B_1$ , while the intensities  $I_2^0$  and  $I_2^h$  include the relative intensity factor  $B_2$  of the initial intensity distribution. As is shown in the lower part of the Figure 3, we have  $I_1^0 + I_2^h > I_2^0 + I_1^g$  due to the initial intensity distribution with  $B_2 > B_1$ .

Summarizing the two-beam analysis above, for the direction  $\vec{u}_2$  of point  $P_2$ , the reduction of  $I_2^0$  by scattering processes away from the higher intensity direction  $B_2(\vec{u}_2)$  cannot be compensated by back-reflected intensity from  $B_1(\vec{u}_1)$  which is redirected towards  $\vec{u}_2$  by  $\vec{g}$ . Conversely, more intensity  $I_2^h$  is scattered towards  $P_1$  by  $\vec{h} = -\vec{g}$ , coming from the higher intensity direction  $B_2(\vec{u}_2)$ , than is scattered away from the direct line along  $B_1(\vec{u}_1)$ . In an extreme case, at a crystal thickness of a quarter of the extinction distance, and neglecting absorption, all intensity is in the diffracted beams and we would have  $I_2^0 = I_1^0 = 0$ ,  $I_1^g = B_1(\vec{u}_1)$ , and  $I_2^h = B_2(\vec{u}_2)$ , leading to the excess and deficit lines with  $I(P_1) > I(P_2)$ , i.e. the relative intensity of the E/D lines is opposite as compared to the initial intensity distribution in the corresponding direct directions.

### 2.2.6. Anomalous Absorption

The redistribution of electrons by dynamical scattering inside a crystal also affects the probability of inelastic scattering [107]. In a crystal, the Bloch waves which show a higher probability at the atomic positions also have a higher probability for inelastic scattering, e.g. the excitation of phonons [97, 108]. In a Kikuchi band, this effect will lead to an increased "absorption" from the diffracted waves for directions with angles less than the Bragg angle. The apparent "absorption" of electrons in a given direction is connected to incoherent large-angle scattering into different directions, i.e. the relevant electrons are not absorbed but only redirected. As has been shown by measurements in the TEM [50–52, 70], with an initially very constricted intensity distribution of an incident beam, the large-angle scattered electrons re-appear in the initially low-intensity regions between and far away from the diffraction spots. Because the large-angle scattering is initiated from atomic positions, the "absorbed" electrons can be assumed to originate from new atomic source positions that produce CPE Kikuchi patterns with high-intensity bands in the pattern regions where there is initially no other background contribution. With increasing sample thickness, however, more and more intensity is also scattered incoherently into larger and larger angles from the incident beam direction by multiple elastic and inelastic scattering events, which will overcome the CPE contrast at some point, ultimately producing a defect band after traversal of a thick crystal region [50–52, 70].

The anomalous absorption effects are not only sources for new CPE patterns, but they will also influence the subsequent diffraction effects in these patterns. For the EBSD CPE patterns, the resulting Kikuchi band contrast reversal effect has been simulated in [109], assuming a larger effective depth of backscattering for sample geometries with a steeper incident beam direction and outgoing directions with a large angle relative to the surface normal. In TKD measurements, thickness and angle dependent contrast reversal effects have been observed [90, 66]. An energy resolved study of anomalous absorption effects in Kikuchi bands can be found in [94]. The conclusion from these observations is that the dark Kikuchi bands created by anomalous absorption effects will be the limiting case for both CPE and IDI diffraction from thick crystals, i.e. after complete incoherence of the CPE effects and after decay of any E/D effects due to the equalization of IDI gradients after multiple inelastic scattering.

As we show in Figure 3, the inelastic scattering effects which "absorb" intensity from the dynamical diffraction process in the crystal can be seen as feeding back into the formation of new diffuse sources. The repetition of such absorption cascades should cause CPE patterns in case of localized phonon scattering or contribute to the IDI distribution after plasmon scattering. The phenomenological model discussed below does include such multiple diffuse diffraction processes only in the sense that the effective parameters describe the final result of all the combined multiple scattering effects on the Kikuchi diffraction contrast.

## 3. Simulation Models

### 3.1. Thomas-Humphreys Model of Diffuse Kikuchi Diffraction

If the waves which travel in different directions from the source in Figure 3 are incoherent, then the observed intensity in the detector plane can be described as the superposition of rocking curves, which are weighted according to the relative intensity which is emitted in different directions by the source. This approach has been discussed by Thomas and Humphreys for the case of diffuse scattering in the transmission electron microscope [55, 71, 110], and is also related to the contrast observed in electron Kossel patterns [106]. The theoretical justification for the Thomas-Humphreys model is discussed in [110, 111], Numerically, the Thomas-Humphreys model amounts to the calculation of transmitted dynamical many-beam rocking curves for the wave vectors of a diffuse source intensity distribution, which are independently diffracted by a crystalline region that is characterized by an effective thickness  $d$  in Figure 3.

As is shown in Figure 4a, the intensity along the observation direction  $\vec{u}_P$  is composed of contributions along different scattering pathways for a final wave vector  $\vec{k}_P$ . The first contribu-

tion is due to the wave  $\Psi_0$  of the electrons which are emitted along the direct way  $\vec{k}_P$  according to  $B(\vec{k}_P)$ . Secondly, there can be additional waves  $\Psi_g$  diverted towards  $\vec{k}_P$  from different initial directions  $\vec{k}_g$ . Diffraction by a reciprocal lattice vector  $\vec{g}$  causes scattering of waves from the initial directions  $\vec{k}_g$  towards  $\vec{k}_P$  via  $\vec{k}_P = \vec{k}_g + \vec{g}$ . For an incoherent source, the resulting intensity  $I_P(\vec{u}_P)$  is then given as the sum of individual beam intensities  $\sum_0^g \Psi_h^* \Psi_h$  which travel along the direction of  $\vec{k}_P$  after transmission through the sample.

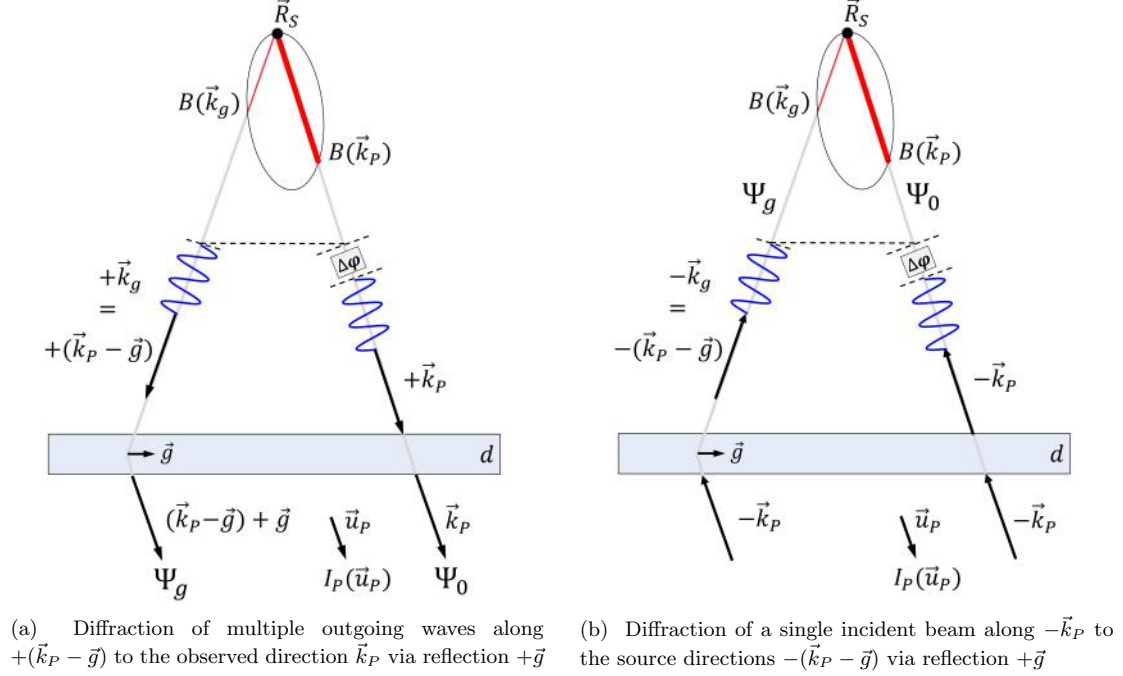


**Figure 4:** Application of the reciprocity principle for simulation of Kikuchi diffraction. The phase shift  $\Delta\phi$  symbolizes the influence of the coherence between the beams with complex amplitudes  $\Psi_0$  and  $\Psi_g$ .

The sum of beam intensities can be calculated using the reciprocity principle for a plane wave beam incident from the detector towards the crystal along  $-\vec{k}_P$ , as is shown in Figure 4b. This beam will be diffracted into beams  $-\vec{k}_g$  towards the diffuse source given by  $-\vec{k}_g = -(\vec{k}_P - \vec{g})$ . Reversing all directions shows that this is equivalent to the sum of intensities emitted from the source along the discrete set of different directions  $\vec{k}_g$  which are contributing to the intensity observed along  $\vec{k}_P$  as shown in Figure 4a.

The directional anisotropy of the source is taken into account by summing the diffracted intensities weighted by  $B(\vec{k}_g)$ , to obtain the intensity  $I_d$  for a crystal of thickness  $d$ :

$$I_d(\vec{k}_P, d) = \sum_g I(-\vec{k}_P - \vec{g}, d) B(\vec{k}_P + \vec{g}) \quad (4)$$

In the experiment, we have to consider a superposition of a distribution of effective incoherent diffuse sources in the sample, according an energy spectrum and a depth distribution, described by a weighting factor  $\rho(E, z)$ :

$$I_P(\vec{u}_P) = \int_{z,E} I_d(\vec{k}_P(E), z) \rho(E, z) dz dE \quad (5)$$

We note that Figure 4 is also relevant for the calculation of CPE patterns [3]. The key difference between the calculation for a CPE pattern emitted from  $\vec{R}_S$  compared to the IDI pattern can be seen for coherent  $\Psi_0$  and  $\Psi_g$  (i.e.  $\Delta\phi$  is fixed) for which the CPE intensity  $\Psi_{CPE}^* \Psi_{CPE}$  is calculated only after summing the complex wave amplitudes  $\Psi_{CPE} = \sum_0^g \Psi_h$ . The source position of  $\vec{R}_S$  introduces phase information into  $\Psi_{CPE}$ . This information is lost for incoherent  $\Psi_0$  and  $\Psi_g$ , i.e. the relative position of  $\vec{R}_S$  in the unit cell does not appear

in the formulas for the IDI Kikuchi features. The transition between the fully coherent and fully incoherent cases can be described by a phenomenological reduction the off-diagonal terms  $\Psi_g^* \Psi_h$ , which describe the interference [112, 113, 94].

### 3.2. Two-Beam Models

Despite a number of simplifying assumptions, the Thomas-Humphreys model discussed in section 3.1 still involves dynamical many-beam calculations for each position of the detection plane, which is computationally too expensive for real-time pattern matching applications. As an approximation to the general many-beam case, two-beam models for Kikuchi pattern formation have been discussed in [72, 81, 86]. Taking into account that, in EBSD patterns, the IDI E/D effects are often a relatively small correction to a dominating CPE Kikuchi pattern, we analyze the application of a two-beam approximation to the Thomas-Humphreys model. As we will show, the two-beam approximation can be the basis for a phenomenological E/D modification of CPE template patterns which are reprojected from a global reference simulation.

#### 3.2.1. Summary of the Analytical Two-Beam Theory with Absorption

In order to motivate the development of a phenomenological model for the diffraction of the incoherent diffuse intensity distribution in Kikuchi patterns, in the following we collect some basic results of the two-beam dynamical theory for diffraction of an incident plane wave beam by an absorbing crystal. For the model of an electron beam with approximately perpendicular incidence on a slab with thickness  $d$ , and the reciprocal lattice vector  $\vec{g}$  of the reflecting lattice plane in the film plane, the analytical result for the transmitted ( $T_g$ ) and reflected ( $R_g$ ) intensities including absorption is well known [107, 108]:

$$T_g = \frac{e^{-\mu_0 d}}{2(1+w^2)} \left[ (1+2w^2) \cosh \frac{\mu_g d}{\sqrt{1+w^2}} \dots \right. \\ \left. + 2w\sqrt{1+w^2} \sinh \frac{\mu_g d}{\sqrt{1+w^2}} \dots \right. \\ \left. + \cos \left( 2\pi \frac{\sqrt{1+w^2}}{\xi_g} d \right) \right] \quad (6)$$

$$R_g = \frac{e^{-\mu_0 d}}{2(1+w^2)} \left[ \cosh \frac{\mu_g d}{\sqrt{1+w^2}} \dots \right. \\ \left. - \cos \left( 2\pi \frac{\sqrt{1+w^2}}{\xi_g} d \right) \right] \quad (7)$$

$$w = \xi_g \cdot S_g \quad (8)$$

$$S_g = \frac{-2K_g g - g^2}{2K} \quad (9)$$

$$\xi_g = \frac{1}{\lambda U_g} = \frac{K}{U_g} \quad (10)$$

$$\mu_g = 2\pi \frac{U'_g}{K} = 2\pi \frac{1}{\xi'_g} \quad (11)$$

$$\mu_0 = 2\pi \frac{U'_0}{K} = 2\pi \frac{1}{\xi'_0} \quad (12)$$

The parameters in the equations above have their usual meanings as described in [108] (equations 7.81, 7.82). The excitation error  $S_g$  is defined as a function of the component  $K_g = \vec{K} \cdot \vec{g}$  of the incident wave vector  $\vec{K}$  along the respective reciprocal space vector  $\vec{g}$  with  $|\vec{g}| = g$ . The Bragg condition is characterized by  $K_g = g/2$  resulting in  $S_g = 0$  and  $w = 0$ . The crystal potentials  $U$  for elastic scattering and for absorption enter into the equations above via the extinction distances  $\xi_g$  and  $\xi'_g$ . The absorption coefficients  $\mu$  are determined from the  $\xi'$ . Due to the absorption effects, one has  $T_g + R_g \neq 1.0$  in the analytical two-beam model.

For a transfer of these analytical results to measurements on a two-dimensional area detector, it can be helpful to remember that the curves for  $T_g$  and  $R_g$  are often shown on a common plot as a function of the deviation parameter  $w$  [108]. Experimentally, however, the transmission  $T_g$  is measured for an incident plane wave beam in a given direction  $\vec{K}_0$ , but the reflected signal  $R_g$  would occur in a different direction, which is determined by the Bragg reflection described by  $\vec{g}$  (i.e. the curves for  $T_g$  and  $R_g$  would be measured by two individual detector pixels in the corresponding directions, which differ by twice the Bragg angle). For a fixed detection pixel, and for a continuous diffuse source intensity distribution, we have a combination of "out-reflection" of intensity away from the pixel (described by the relevant  $T_g$  of lattice planes  $g$  near the Bragg angle) combined with "in-reflection" towards the detector pixel from various other initial directions (described by  $R_h$  of *different* lattice planes  $h$ ), plus the effect of absorption processes.

### 3.2.2. Phenomenological Model of E/D Effects

For the description of excess-deficiency effects in EBSD patterns, we now derive a phenomenological model which is based on the two-beam approximation to dynamical diffraction as described in the previous section. As a first approximation, we assume that under the experimental conditions which are relevant for EBSD Kikuchi patterns, the thickness oscillations described by the  $+/-$  cos-terms in equations 6 and 7 are averaged out and can be neglected. Moreover, we assume that the remaining parameters in equations 6 and 7 are purely phenomenological parameters which can be used to fit an experimental intensity distribution. The excess-deficiency effects of the IDI distribution are assumed to be a small additional signal relative to a main CPE signal, and the phenomenological model estimates the changes relative to an underlying mean intensity (relative to the mean absorption, i.e. taking  $\mu_0 = 0$ ).

The phenomenological profile shapes can be described with effective parameters in correspondence to equations 6 and 7:

$$t_g(\vec{u}_P) = B(\vec{u}_0) \cdot \frac{e^{-\mu_0 d_{\text{eff}}}}{2(1 + w_g^2)} \left[ (1 + 2w_g^2) \cosh \frac{\mu_g d_{\text{eff}}}{\sqrt{1 + w_g^2}} \dots \right. \\ \left. + 2w_g \sqrt{1 + w_g^2} \sinh \frac{\mu_g d_{\text{eff}}}{\sqrt{1 + w_g^2}} \right] \quad (13)$$

$$r_h(\vec{u}_P) = B(\vec{u}_h) \cdot \frac{e^{-\mu_0 d_{\text{eff}}}}{2(1 + w_h^2)} \left[ \cosh \frac{\mu_h d_{\text{eff}}}{\sqrt{1 + w_h^2}} \right] \quad (14)$$

$$\vec{u}_0 = \frac{\vec{k}_P}{|\vec{k}_P|} \quad (15)$$

$$\vec{u}_h = \frac{\vec{k}_P - \vec{h}}{|\vec{k}_P - \vec{h}|} \quad (16)$$

$$w_q = w_r \cdot \xi_q \cdot S_q \quad (q = g, h) \quad (17)$$

For the discussion of the complete set of model parameters in addition to equations 13 and 14, see section 3.3.

The two-beam formulas allow to describe a number of key mechanisms which are relevant for the diffraction of the incoherent diffuse intensity distribution. This will be shown in the following, by discussing simulations of Kikuchi band profiles for different simplified situations.

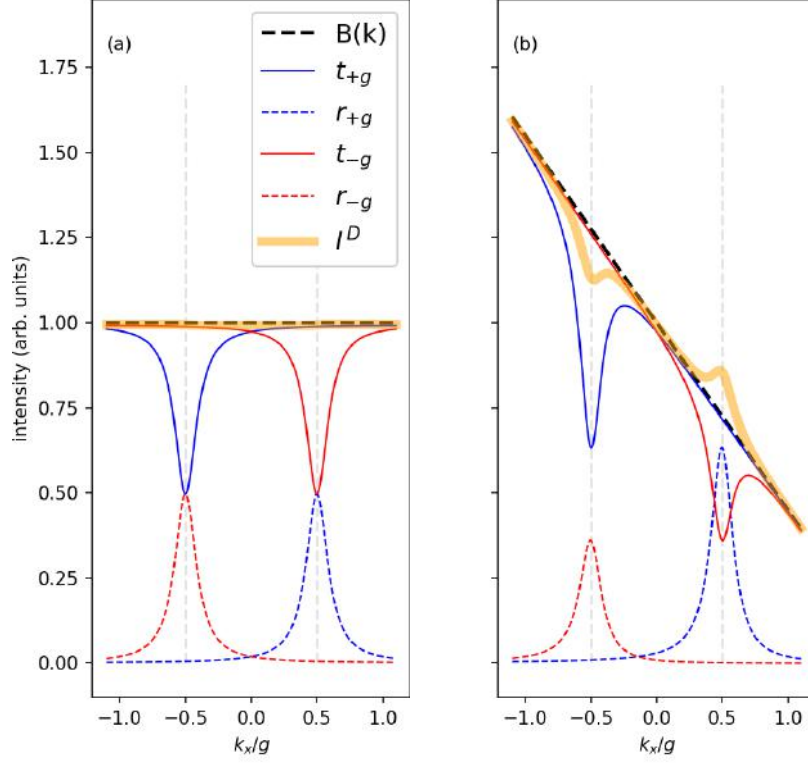


**Figure 5:** Role of the source intensity gradient in the phenomenological two-beam model. Low effective thickness  $d = 0.001\xi'_g$  (minor absorption effects). (a) The constant source intensity  $B(k_x) = 1.0$  leads to exact compensation of the intensities scattered from  $k_x = -0.5$  to  $k_x = +0.5$  and vice versa in the final intensity  $I^D = (t_{+g} + r_{-g} + t_{-g} + r_{+g})/2$ , (b) In case of a changing source intensity  $B(k_x) = 1.0 - 0.55k_x$ , more intensity is scattered from  $k_x = -0.5$  towards  $k_x = +0.5$  than the other way. This leads to the excess and deficiency lines in the final intensity  $I^D$  near the Bragg angles. Example parameters:  $|g| = 1$ ,  $|K| = 1$ ,  $\xi_g = 10/|g|$ ,  $\xi'_g/\xi_g = 10$ ,  $\xi'_0/\xi_g = 10$ .

The first case is shown in Figure 5, which describes a situation of low thickness, for which absorption does not play a dominant role. In panel (a) of Figure 5, the source intensity  $B(k)$  is assumed to be constant. Bragg reflections occur at  $k_x/g = \pm 0.5$ , corresponding to scattering by  $\pm g$ . Considering first the position  $k_x/g = -0.5$ , we can see that at the positions of this Bragg reflection, two processes contribute to the final diffracted intensity  $I^D$ : firstly, the solid blue line for  $t_g$  describes a reduction of intensity in this direction due to reflection of intensity *away* from  $k_x/g = -0.5$  via scattering by  $+1g$ . Secondly, at  $k_x/g = -0.5$  there is also the additional intensity of  $r_{-g}$ , which is reflected *towards* this direction from the initial diffuse intensity  $B$  along  $k_x/g = +0.5$  due to the reciprocal vector  $-1g$ . Similarly, the final intensity at  $k_x/g = +0.5$  is determined in a completely symmetric way (i.e. we assume that scattering by  $+g$  and by  $-g$  is equally strong, i.e. for a centrosymmetric potential). In effect, Figure 5(a) describes a final situation where as much intensity is scattered away from a given direction as is scattered towards it, and the final intensity curve  $I^D$  appears the same as it would without any diffraction at all. In this sense, the smooth background intensity can be the result of compensating diffraction components due to an isotropic part  $B(k) = \text{const}$  in the initial diffuse intensity.

In comparison to a constant  $B(k)$  in Figure 5(a), the result of a gradient in  $B(k)$  is characteristically different, as shown in Figure 5(b) for a linearly changing  $B(k)$  in the region of the



Kikuchi band. Now, the detailed balance between the intensity scattered away and towards a direction, respectively, is influenced near the Bragg reflections by the different intensities at  $B(k_x/g) = -0.5$  compared to  $B(k_x/g) = +0.5$ . As can be seen in Figure 5(b), slightly more intensity is scattered from  $k_x/g = -0.5$  towards  $k_x/g = +0.5$  because the initial intensity is higher at  $B(k_x/g) = -0.5$  relative to  $B(k_x/g) = +0.5$ . As a result, in agreement with the experimental observation, the phenomenological model treats the appearance of a deficient line at that edge of a Kikuchi band, which is oriented towards an increasing diffuse background intensity, whereas an excess line appears at the edge oriented towards the decreasing background. With respect to the experiment, Figure 5(a) corresponds to bands which are oriented in such a way, that there is no gradient in the diffuse intensity for the  $-g$  and  $+g$  reflections, which, for the tilted samples used in EBSD, is in the plane described by the incident beam and the surface normal, i.e. these bands appear to run nearly vertical in an experimental pattern. As seen from the position of the EBSD camera, the diffuse background intensity scattered from the sample changes much less from left to right than from top to bottom. We note that the actually measured distribution of the intensity in the detected raw EBSD pattern is also influenced by gnomonic projection effects changing the solid angle captured by each pixel, which does not cause E/D asymmetries.

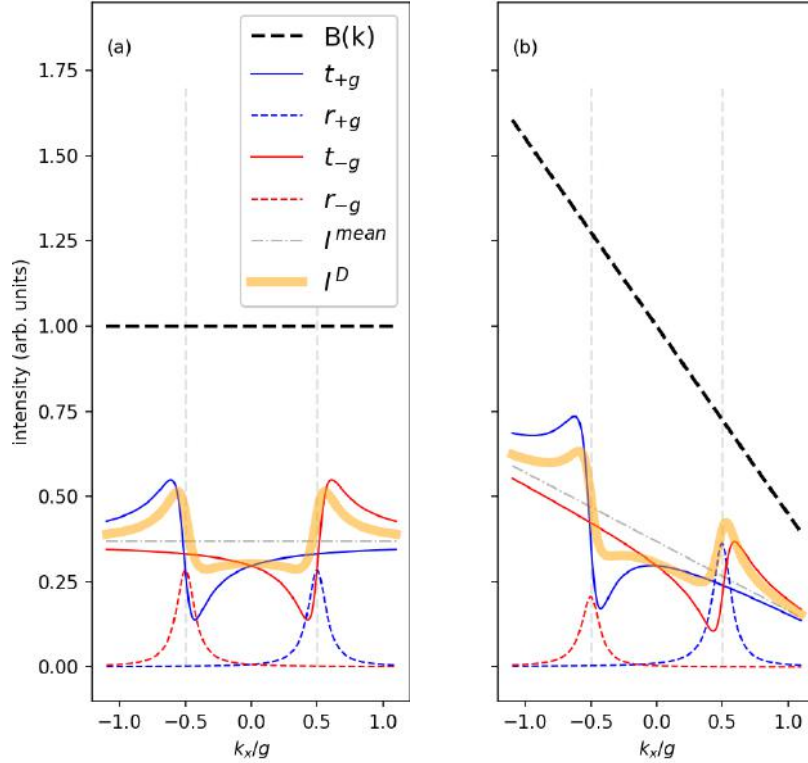


**Figure 6:** Role of absorption for excess-deficiency effects at increased effective thickness  $d_{\text{eff}} = \xi'_0/2\pi$  (i.e.  $\mu_0 d_{\text{eff}} = 1$ ,  $I^{\text{mean}} = \exp(-1.0) \approx 0.37$ , all other parameters as in Fig. 5). Now, even in case (a) of a constant incident intensity  $B(k_x) = 1.0$ , a defect band will be caused by anomalous absorption as controlled by the values of  $\xi'_g$ . (b) A gradient in the source intensity leads to a defect band combined with excess-deficiency features, relative to the mean remaining intensity  $I^{\text{mean}}$ , which would be transmitted through an amorphous sample of thickness  $d_{\text{eff}}$ .

Figure 6 shows the corresponding Kikuchi band profiles from Figure 5 when significant absorption is relevant, i.e. for a thicker sample. First of all, absorption leads to a reduction of the mean level of the transmitted intensity  $I^{\text{mean}}$ , which would be observed for an amorphous sample. The inclusion of anomalous absorption effects, which are related to the crystal structure, shows in Figure 6(a) that the intensity reduction is slightly stronger for directions smaller than the Bragg angles ( $-0.5 < k_x/g < +0.5$ ), while the electrons are absorbed somewhat less for angles slightly larger than the Bragg angle ( $|k_x/g| > +0.5$ ). This leads to the formation of a

band of lower intensity for transmitted electrons in thick samples, which is additionally modified by excess-deficiency effects as shown in Figure 6(b). Similar to Figure 5(b) discussed above, the non-compensated scattered intensities are caused by the gradient in the IDI distribution.

In summary, the phenomenological model based on the formulas 13 and 14 is able to approximate the key effects related to excess-deficiency features in Kikuchi patterns. The curves of Figure 5 and Figure 6 also show qualitative agreement with those presented in [72] using a more detailed two-beam theory.

### 3.3. Improved Model for Simulation of EBSD Kikuchi Patterns

Formulas 13 and 14 enter into an improved model to simulate Kikuchi patterns observed in EBSD and TKD, which considers the following parameters:

1. the projection center  $\mathbf{PC} = (PCX, PCY, PCZ)$ , determined by the beam position of the SEM relative to the detection screen
2. the crystal orientation  $\hat{\mathbf{o}}$  relative to the detection screen, as described, for example, by Euler angles  $\hat{\mathbf{o}} = (\phi_1, \Phi, \phi_2)$
3. the parameters entering the simulation of the CPE Kikuchi pattern as described in [2, 3], for an effective kinetic reference energy  $E_{\text{kin}}^0$
4. a relative intensity correction of the CPE pattern due to diffraction of the IDI background intensity. This can be approximated by a phenomenological two-beam model using equations 13 and 14 for a number of relevant reciprocal lattice vectors  $\vec{g}$ :

$$S_{IDI}(\vec{u}_P) = \sum_g [t_g(\vec{u}_P) - 1.0] + r_{-g}(\vec{u}_P) \quad (18)$$

The signal  $S_{IDI}$  in direction  $\vec{u}_P$  in the final Kikuchi pattern is composed of two contributions for each reflection  $g$ :

- a deficient intensity (negative relative to the intensity after the mean absorption for an amorphous sample)  $t_g(\vec{u}_P) - 1.0$ , which describes the reduction of the diffuse intensity going towards  $\vec{u}_P$  by the reflection  $+\vec{g}$  away from  $\vec{u}_P$  and additional anomalous absorption related to  $+\vec{g}$ .
- an excess intensity due to diffuse intensity which is initially not going towards  $\vec{u}_P$  but which is redirected from the direction  $\vec{u}_{-g}$  by Bragg reflection  $-\vec{g}$  towards the pattern pixel in direction  $\vec{u}_P$

When features due to different  $\vec{g}$  overlap, the possible multiple-beam interference effects are neglected in a two-beam approximation. The inclusion of many-beam effects in the diffraction of the IDI distribution,  $S_{IDI}(\vec{u}_P)$  is possible using the Thomas-Humphreys-Model discussed in section 3.1.

5.  $S_{IDI}$  depends on the anisotropic diffuse intensity distribution of the background  $B(\vec{u})$  as a function of the unit vector  $\vec{u}$  along the detection direction. We parameterize  $B(\vec{u})$  using a reference direction  $\vec{u}_M$  which describes the direction with the intensity maximum, while an exponent  $a$  describes the change of intensity with increasing deviation of the detection direction  $\vec{u}$  from the reference direction  $\vec{u}_M$ :

$$B_1(\vec{u}) = \left( \frac{1 + \vec{u} \cdot \vec{u}_M}{2} \right)^{a_1} \quad (19)$$

The reference direction  $\vec{u}_M$  can be parameterized in polar coordinates relative to the sample surface normal, e.g.  $\vec{u}_M = (u_\theta, u_\phi)$ . With this functional form for  $B$ , we have

$B(\vec{u}) = 1$  along  $\vec{u} = \vec{u}_M$ , decreasing to  $B(\vec{u}) = 0$  for  $\vec{u} = -\vec{u}_M$  and  $a > 1$ . The shape of  $B(\vec{u})$  can be adjusted to different experimental conditions, i.e. for a very sharp intensity distributions, exponential functions could be more suitable [71]. We have used the following function  $B_2(\vec{u})$  to describe the sharp intensity distributions which lead to spot-like diffraction patterns, i.e. a situation in which a multiple scattering has not yet broadened the intensity to cause significant overlap of diffraction orders:

$$B_2(\vec{u}) = \exp[a_2(\vec{u} \cdot \vec{u}_M)] \quad (20)$$

In general situations, it needs to be considered that  $B$  can depend on the depth and energy, for example,  $B(\vec{u}) = B(\vec{u}, E, d)$ , as determined by a progressing beam broadening due to multiple elastic and inelastic scattering in the sample.

6. Parameters describing the diffraction effects of the diffuse intensity using an analytical two-beam approximation:
  - the scaling factor  $e_D$  to describe the effective kinetic energy of the diffuse intensity relative to the nominal primary beam energy  $E_0$
  - the effective thickness  $d_{\text{eff}}$  of the diffracting region, also scales the absorption effects, thickness fringes are not considered by this model, it is assumed that these are averaged out
  - a scaling factor  $w_r$ , adjusting the deviation parameter  $w$  from the exact Bragg condition at  $w = 0$ , which allows to control the width of the Kikuchi features near the Bragg lines
7. The relative weight  $m_D$  of the diffuse E/D contribution to the final diffraction pattern. The final pattern signal  $S_K$  is given by adding the contribution  $S_{CPE}$  of the CPE Kikuchi pattern and the contribution  $S_{IDI}$  due to diffraction of the diffuse intensity as

$$S_K = (1 - m_D)S_{CPE} + m_DS_{IDI} \quad (21)$$

The signals  $S_{CPE}$  and  $S_{IDI}$  are considered to be normalized e.g. to zero mean and unit standard deviation.

8. Experimental Kikuchi features are often well described by a simulation at a single effective energy, combined with a reduction in feature sharpness handled by a convolution filter [42]. A Gaussian smoothing filter with parameter  $\sigma_G$  is assumed to treat effects of the electron energy spectrum on  $S_K$ , as well as additional optical blurring effects in the detector.

In the model above, the asymmetries due to the E/D effects are controlled by the differences of the background intensity (equations 19 and 20) for different observation directions. In the absence of such background gradients, E/D effects are not introduced by other parameters, i.e. the two-beam approximation effects and image processing by gaussian blurring do not introduce asymmetries by themselves.

For pattern matching applications, the phenomenological correction parameters will need to be calibrated on a known sample and kept constant during fitting of the crystallographic parameters of the orientation, projection center, or strain for an experimental EBSD map.

## 4. Applications

### 4.1. Projection Center Accuracy for EBSD

As a first application, we discuss the systematic errors which are introduced by neglecting E/D effects in EBSD pattern simulations.

#### 4.1.1. Experimental Details

The experimental Kikuchi diffraction pattern was obtained from a troilite (FeS) inclusion found in a sample from the Canyon Diablo iron meteorite [114]. The sample used in this study was prepared using standard procedures, and the measurements have been performed using a field-emission gun scanning electron microscope (FEG-SEM) LEO 1530VP (Zeiss, Germany). Using the high-current mode and a 120  $\mu\text{m}$  aperture, the Shottky field emitter delivered a probe current of about 10...12 nA in high vacuum mode.

For the EBSD-pattern acquisition an  $e^-$ Flash<sup>HR</sup> (Bruker, nominal CCD-chip resolution: 1600  $\times$  1200 pixels) was used. The analyzed pattern has a dimension of 400 $\times$ 288 pixels (top clipping of the upper 5% of lines due to hardware limitations of the detector type).

The crystal structure of troilite was assumed in the hexagonal space group  $P\bar{6}2c$  (International Tables no. 190), with lattice parameters  $a = 5.9650 \text{ \AA}$  and  $c = 11.7570 \text{ \AA}$  as given in [115]. The dynamical simulation included 877 beams, selected according to a minimum lattice spacing of  $d_{\text{hkl}} > 0.4 \text{ \AA}$  and a structure factor amplitude of more than 20% relative to the strongest reflection. The calculations were carried out using the implementation of the Bloch wave approach as described in [3]. We used the conventions for the orientation (Euler angles) and projection center as given in [116].

Model parameters were determined via fitting to the experimental Kikuchi pattern, as described in [24, 25]. The best fit parameters were determined at the maximum of the normalized cross correlation coefficient (NCC) between the simulated pattern and the experimental pattern. In comparison to other available measures used for Kikuchi pattern matching, the NCC is very robust to changes in brightness and contrast in the analyzed Kikuchi patterns, among other useful properties of the NCC [117–120]. The pattern matching procedure compares background-corrected Kikuchi patterns which have been normalized to a mean of zero and unit standard deviation [42]. As starting values for the optimization procedure, we used the values of the local orientation and PC as given by the EBSD system software (Bruker Esprit 1.94). The starting values were optimized using the Nelder-Mead (NM) algorithm as implemented in the NLOPT non-linear optimization package [121].

#### 4.1.2. Quantitative Pattern Fits

In Figure 7, we show an experimental Kikuchi diffraction pattern of troilite, with crystallographic features indexed in a gnomonic projection. Assuming a perfect gnomonic projection without additional distortions, the basic task of the geometrical calibration is to determine the coordinates of the corner pixels of the experimental pattern in the coordinate system Figure 7 with the projection center at (0,0). The angles  $\rho_G$  relative to the direction at (0,0) can then be calculated via  $r_G = \sqrt{x_g^2 + y_g^2} = \tan \rho_G$ , which enables the calculation of interplanar angles between Kikuchi bands. Concerning the E/D effects discussed in Figure 1, we see in Figure 7 that bands with a strong E/D asymmetry are oriented in such a way that they show a large angle with the vertical direction of the pattern. Such bands include, for example, the  $(1\bar{2}1)$ ,  $(2\bar{1}0)$ ,  $(2\bar{1}2)$ , and  $(116)$  bands. In agreement with this observation, a very strong E/D-effect is seen for the horizontally running  $(\bar{1}10)$  band at the lower edge of the pattern, with the  $[001]$  zone axis in the center. At the  $[001]$  direction, the nearly vertical  $(110)$  band is crossing, which does not appear to show any pronounced E/D asymmetry, as is also indicated by the "N" label in Figure 1.

In Figure 8, we show the effect of three types of best-fit simulations for the experimental troilite pattern with a resolution of 400 $\times$ 288 pixels. The image similarity is seen to increase considerably from a normalized cross-correlation coefficient of  $r = 0.7433$  for the CPE Kikuchi pattern simulation without any E/D effects (left column), to  $r = 0.8410$  for the two-beam diffuse intensity correction model discussed above (TBD, center column), and  $r = 0.8640$  for the many-beam Thomas-Humphreys model (MBD, right column). The increase of the NCC due to an improved agreement of pattern features can be seen also in the lower row by the reduction of red-blue contrast which indicates the differences between the experimental pattern





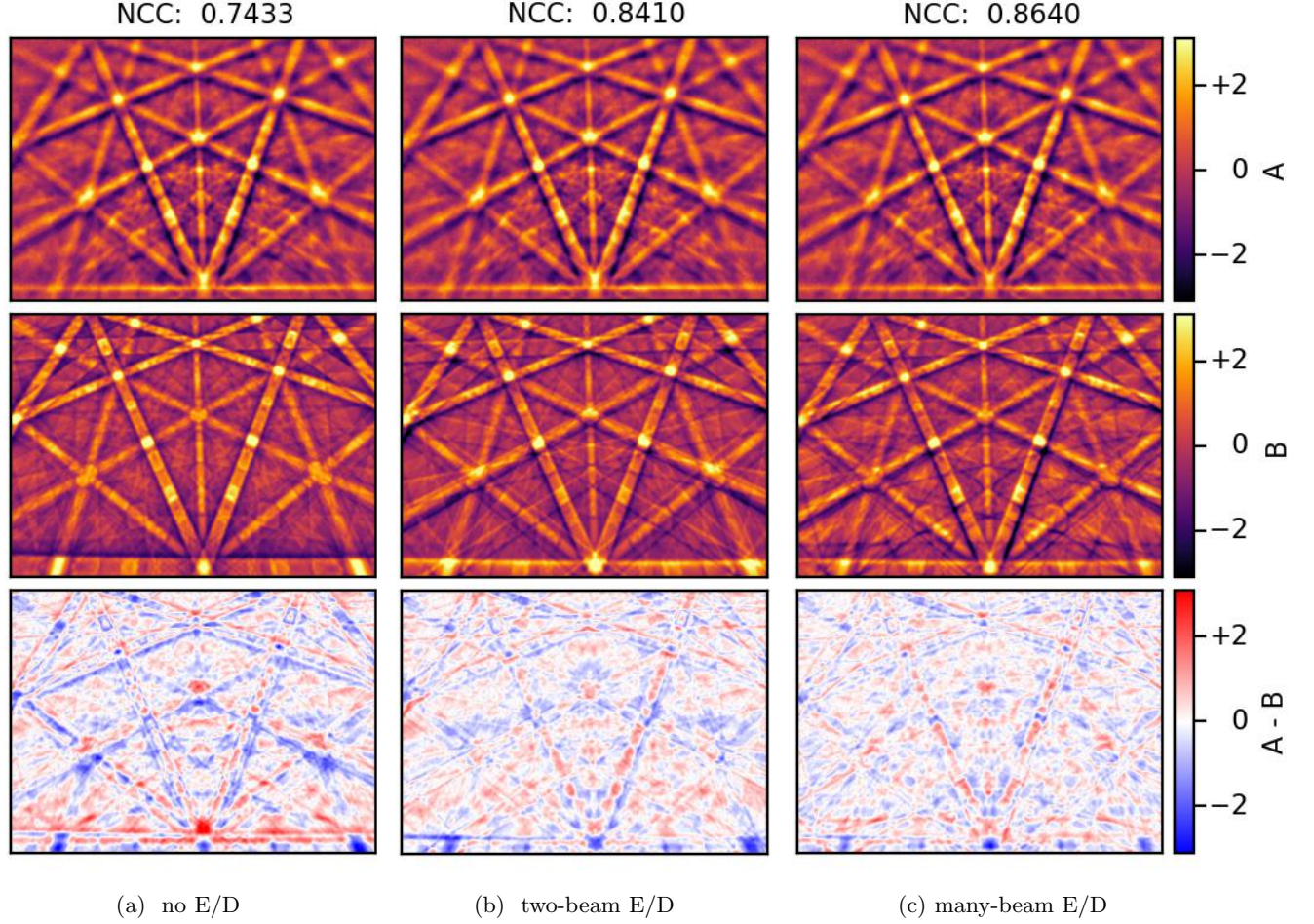


**Figure 8:** Comparison of the experimental Kikuchi pattern from troilite (top row) to the simulated diffraction signals  $S_Q$  (middle row), and the difference between experiment and simulation (bottom row). Reference energy:  $E_{\text{kin}}^0 = 20.7 \text{ keV}$ , Gaussian blur fixed at  $\sigma_G = 1.0 \text{ px}$  (a) Simulation without E/D effects (CPE), best-fit normalized cross correlation coefficient (NCC)  $r = 0.7433$ ,  $\hat{\mathbf{o}}_1 = (4.454^\circ, 44.706^\circ, -33.537^\circ)$ ,  $\mathbf{PC}_1 = (0.48362, 0.18091, 0.79753)$ ; (b) Simulation including E/D effects in two-beam model (TBD),  $r = 0.8410$ ,  $\hat{\mathbf{o}}_2 = (4.495^\circ, 44.630^\circ, -33.452^\circ)$ ,  $\mathbf{PC}_2 = (0.48394, 0.19125, 0.80174)$ ; (c) Many-beam model of E/D effects (MBD),  $r = 0.86$ ,  $\hat{\mathbf{o}}_3 = (4.356^\circ, 44.663^\circ, -33.356^\circ)$ ,  $\mathbf{PC}_3 = (0.48589, 0.19197, 0.80412)$ ;

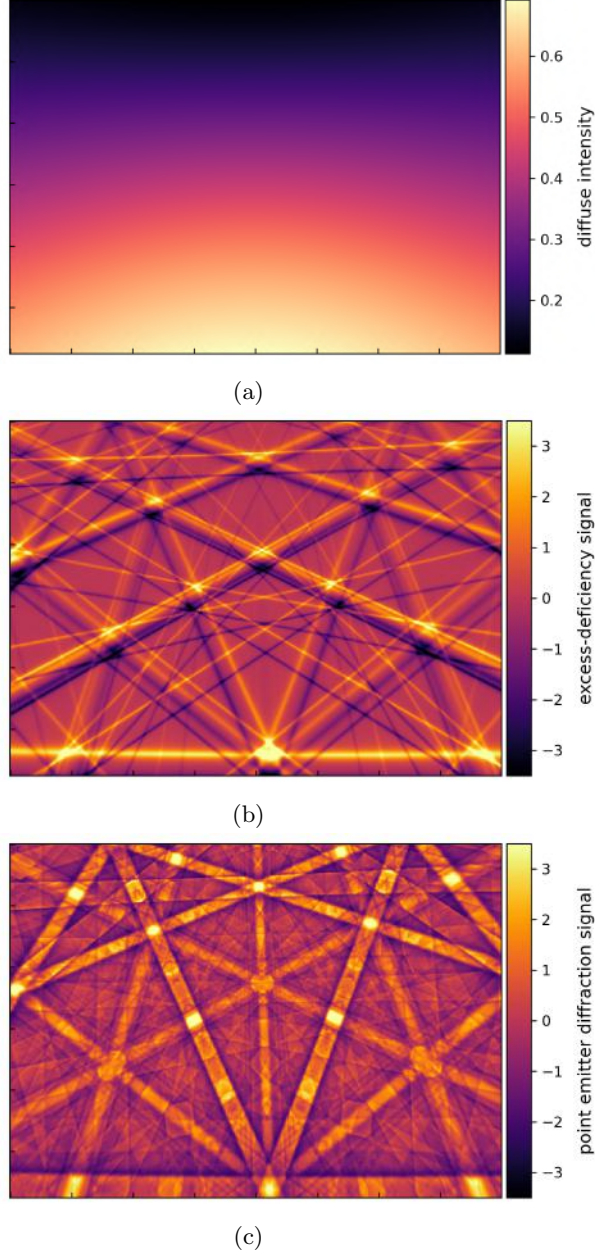


**Figure 9:** The signal contributions to the best-fit simulated pattern in Fig.8. (a) diffuse background  $B(\vec{u})$ ; (b) two-beam excess-deficiency correction signal  $S_{IDI}$  resulting from the diffuse background in (a); (c) Kikuchi diffraction signal  $S_{CPE}$  due to localized backscattering.

(top row) and the simulated patterns (middle row).

The residuals of the pattern fits such as shown in Figure 8 are dominated by the strongest Kikuchi bands, as can be seen by the magnitude of the red and blue difference features, which can be attributed to specific (hkl) bands in Figure 7. In such a case, the E/D effects on the strongest bands are the most important for adjusting the orientation and the projection center. In Figure 9, we show the diffuse background distribution (a) which was assumed for the two-beam correction involving the strongest Kikuchi bands (b), which is added to the full many-beam CPE simulation (c), resulting in the simulated pattern in the center panel of Figure 8. The over-emphasized regions with the highest and lowest intensities in the pattern are caused by the neglect of the many-beam interference at the crossing regions of Kikuchi band edges. However, the two-beam approximation to the effects in the strongest bands could be acceptable if the influence of E/D effects is still relatively low for an investigated phase. A restriction of the two-beam correction to the strongest bands could be important for real-time corrections of CPE pattern templates using parallel hardware acceleration on GPUs.

The best-fit parameters of the different simulations are summarized in Table 1. The parameter  $m_D$  indicates that the E/D signal is in the order of 10% compared to the CPE pattern.

Parameters	CPE	TBD	MBD
NCC $r$	0.7433	0.8410	0.8640
$\phi_1$	4.454°	4.495°	4.356°
$\Phi$	44.706°	44.630°	44.663°
$\phi_2$	-33.537°	-33.452°	-33.356°
$PCX$	0.48362	0.48394	0.48589
$PCY$	0.18091	0.19125	0.19197
$PCZ$	0.79753	0.80174	0.80412
$m_D$	0.0	0.09	0.10
$e_D$	-	1.07	1.06
$u_\theta$	-	91°	115°
$u_\phi$	-	0.3°	7.2°
$a_1$	-	2.2	2.6
$d_{\text{eff}} (\text{\AA})$	-	10	-
$w_r$	-	0.8	-

**Table 1:** Best fit parameters of the different Kikuchi pattern simulations shown in Fig. 8 (TBD: two-beam E/D correction, MBD: many-beam E/D correction, CPE: Kikuchi pattern without E/D effects).

#### 4.1.3. Accuracy of Projection Center Coordinates

In order to judge the systematic changes in the geometrical calibration of the experimental pattern which would result from using the different simulation models, we show the differences of the projection center coordinates  $PCX$ ,  $PCY$ ,  $PCZ$  in Table 2, which also includes the misorientation angle  $\omega_{\text{MO}}$  between the respective best-fit orientations.

Models	$\Delta PCX$	$\Delta PCY$	$\Delta PCZ$	$\omega_{\text{MO}}$
TBD - CPE	0.32	10.3	4.2	-2.4
MBD - CPE	2.2	11.0	6.6	-2.4
MBD - TBD	1.9	0.72	2.4	1.8

**Table 2:** Differences in projection center coordinates  $\Delta PCX$ ,  $\Delta PCY$ ,  $\Delta PCZ$  (in units of  $10^{-3}$ ) and misorientation angles  $\omega_{\text{MO}}$  (in units of  $10^{-3}$  rad) which result from the best fit parameters of the different Kikuchi pattern simulations shown in Fig. 8 (TBD: two-beam E/D correction, MBD: many-beam E/D correction, CPE: no E/D effects).



From Table 2, we can see the largest changes of the projection center in the Y-component, with  $\Delta PCY = 10.3 \times 10^{-3}$  for the two-beam E/D model (TBD) and  $\Delta PCY = 11.0 \times 10^{-3}$  for the many-beam MBD simulation. Because we use the convention of [116], the positive value of  $\Delta PCY$  means that  $PCY$  is shifted down in the pattern for the TBD and MBD models compared to the CPE model. The vertical down-shift of the best-fit PC in the image when including the E/D effects can be explained by the experimentally asymmetric Kikuchi band intensity in the vertical direction, i.e. the intensity of the inclined bands is shifted towards the top of the pattern. In such a case, a simulated model which does not include E/D effects will tend to shift its symmetric bands also slightly upwards, explaining the dominating  $y$ -shift in the projection center coordinates. Quantitatively, for the example pattern discussed here, the fit using the conventional CPE simulation model would thus estimate a  $PCY$  which is shifted upwards by about 1% of the pattern height compared to the better fits when including the E/D effects. The changes in the other two PC coordinates are smaller, but they still have magnitudes of a few times  $10^{-3}$ .

We also see from Table 2, that the best-fit orientation changes in connection with the PC, as is quantified by misorientation angles  $\omega_{MO} = -2.4 \times 10^{-3}$  rad ( $0.14^\circ$ ) between the fitted orientations with and without E/D effects. The simulation models between themselves show differences up to  $\Delta PC = 2.4 \times 10^{-3}$ , while the misorientation angle is of similar magnitude  $\omega_{MO} = 1.8 \times 10^{-3}$  rad than the change between CPE vs. TBD/MBD models.

Assuming the best-fit MBD simulation ( $r = 0.8640$ ) as the reference, a neglect of the E/D effects in the Kikuchi pattern simulation thus can show a systematic shift of up to  $\times 10^{-2}$  in the  $PCY$  coordinate, and shifts in the order of a few  $\times 10^{-3}$  in the  $PCX$  and  $PCZ$ , with similar systematic changes of the orientations as characterized by the misorientation angles  $\omega_{MO}$  of about  $2 \times 10^{-3}$  rad.

In [122] it has been estimated that an uncertainty of 0.005 in the projection center results in uncertainty of about  $10^{-3}$  in the strain state, i.e. a variation of 0.1% in lattice parameters. A similar estimation can be obtained from elementary geometry [123], i.e. the uncertainty of the PC relative to the screen size is roughly equivalent to the uncertainty of lattice parameter ratios. In view of the systematic shifts observed for different simulation models, this corresponds to possible phantom strains in the order of  $10^{-3}$  to  $10^{-2}$  when E/D effects are neglected.

#### 4.2. Pattern Matching for Transmission Kikuchi Diffraction

We also tested the application of our simulation model to Kikuchi diffraction measurements in a transmission geometry in the SEM, which can pose specific challenges in an on-axis geometry [65–68] due to the possible strong contribution of the transmitted incident beam for thin samples.

In Figure 10, we show simulations for the TKD pattern of Magnesium, measured at 30kV from a sample thickness of 200 nm [66], as reproduced in Figure 2(a). The central area has been masked due to the presence of strong diffraction spots from the incident beam, and the outer areas have been masked due to increased noise.

We compare a conventional CPE simulation in Figure 10(a) to an improved simulation in Figure 10(b) which includes E/D effects treated by the Thomas-Humphreys model discussed above. The respective cross-correlation coefficients are calculated only for the pattern area which is not masked, and show a clear improvement from  $r = 0.7441$  for the CPE simulation, to  $r = 0.7983$  for the simulation considering E/D effects. The most important qualitative difference of on-axis TKD measurements to the backscattering geometry is the centrally peaked distribution of the background intensity, which leads to a radial gradient that correspondingly causes deficiency features for the Kikuchi band edge nearer to the incident beam in the center of the pattern, and excess features on the corresponding outward band edge. The appearance of these radial E/D effects is successfully reproduced by the simulation in Figure 10(b), which can also be seen by the noticeable reduction in red-blue contrast of the residual difference pattern.

The best-fit parameters for the simulations in Figure 10 are shown in Table 3. The concentration of intensity in the central part of the pattern is seen by the large exponent  $a_2 \approx 40$  needed in the background intensity model, compared to a much flatter background in the backscatter measurements. Also for the case of TKD we find considerable systematic shifts in the PC coordinates between the two simulation models used for pattern fitting. In the case of the analyzed TKD pattern, the *PCZ* coordinate (i.e. the "camera length" in a TEM) is most strongly affected, with a shift in the order of a few times  $10^{-3}$ . The misorientation angle between the corresponding sample orientations is  $0.074^\circ (\approx 10^{-3} \text{ rad})$ .

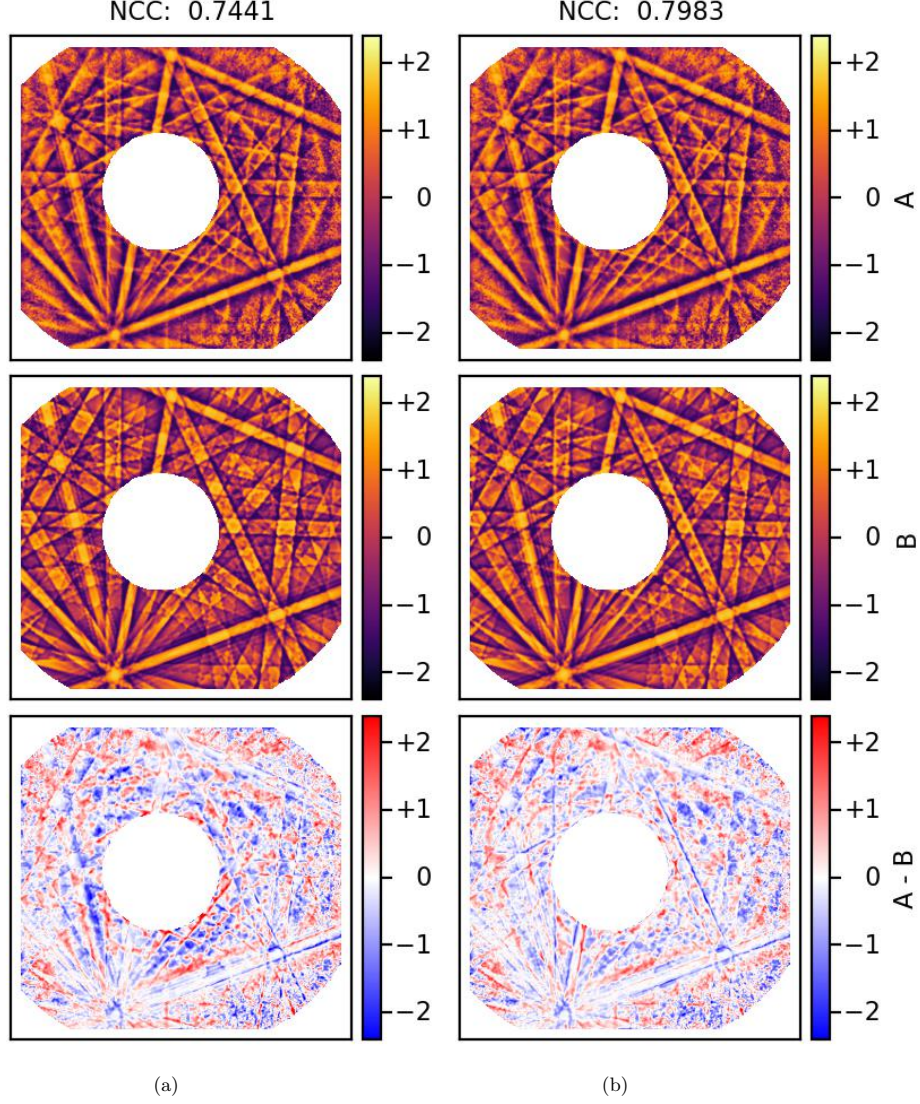


**Figure 10:** Best fit simulations (B) for the experimental Mg TKD pattern (A) of Brodu *et al.* (Fig.7 in [66]). The parameters of the simulations are shown in Table 3. (a) CPE simulation (b) CPE+IDI simulation including E/D effects. The central and outer pattern regions have been masked from the comparison.

Parameters	CPE	MBD	$\Delta$
NCC $r$	0.7433	0.79826	
$\phi_1$	-159.593°	-159.658°	
$\Phi$	68.789°	68.781°	0.074°
$\phi_2$	163.977°	163.960°	
$PCX$	0.44184	0.44160	$-0.24 \times 10^{-3}$
$PCY$	0.490312	0.490308	$-4.4 \times 10^{-6}$
$PCZ$	0.92763	0.92214	$-5.5 \times 10^{-3}$
$m_D$	0.0	0.08	
$e_D$	-	1.03	
$u_\theta$	-	0.05°	
$u_\phi$	-	0.0°	
$a_2$	-	41.3	

**Table 3:** Best fit parameters of the different Kikuchi pattern simulations shown in Fig. 10 (CPE: Kikuchi pattern without E/D effects, MBD: many-beam E/D correction).

#### 4.3. Thickness-dependent Variation of Contrast in Kikuchi Diffraction

The refined simulation model for Kikuchi patterns uses a relatively small number of adjustable phenomenological parameters, but allows to semi-quantitatively reproduce many of the contrast changes that are observed in Kikuchi diffraction patterns in the SEM as well as in the TEM [70].

As an example, we use the geometrical conditions relevant for the TKD pattern of the Mg sample shown in Figure 2a, and, by changing the corresponding model parameters, we describe various stages of the interplay between beam broadening and the dynamical diffraction and absorption with increasing sample thickness. Generally, as we can see in Figure 11, the model can cover the transition from the spot diffraction pattern of a very thin sample and a relatively tightly collimated beam (shown in Figure 11a), to a very broad background intensity with inverted Kikuchi bands for a very thick sample (shown in Figure 11d). We will now discuss this transition in detail.

The situation for the thinnest samples is shown in Figure 11a. A spot diffraction pattern is created by the discrete transfer of momentum from the crystal to a collimated beam, i.e. the incident beam wave vectors all have very similar directions. To model this type of incoherent source intensity, a very high exponent of  $a_2 \approx 5 \times 10^5$  is used in eqn. 20. This choice leads to an effective beam divergence of about 10 mrad which describes the size of the spots in the experimental diffraction pattern of Figure 2a. We assumed a perpendicularly incident beam for simplicity, and did not optimize the exact beam divergence or the angle of incidence for the spot pattern in Figure 11(a). The exact agreement of the spot features to the experimental pattern is hard to estimate due to the necessary overexposure in the central part of the pattern in Figure 2a, but we see the expected spacing of diffraction spots due to the reciprocal lattice of the Mg crystal structure. For future pattern matching applications, it can be envisioned that the increased sensitivity of the spot diffraction pattern to the incident beam direction could be used to determine the relative orientation of the crystal, incident beam and the detector plane.

In Figure 11b, the beam broadening already has become significantly larger than the Bragg angles of the reflections, so that different diffraction orders overlap strongly. The appearance of a discrete, spot-like intensity pattern is lost. Due to the intensity gradient of the IDI distribution, the excess and deficiency features appear as marked by "D" and "E". This situation can be compared to CBED TEM experiments, when diffraction disks can be made to overlap to form an electron Kossel pattern [97]. The overlap in the present case is basically invisible due to the smooth intensity gradients, as compared to the sharply defined disks of the external beam intensity in CBED.

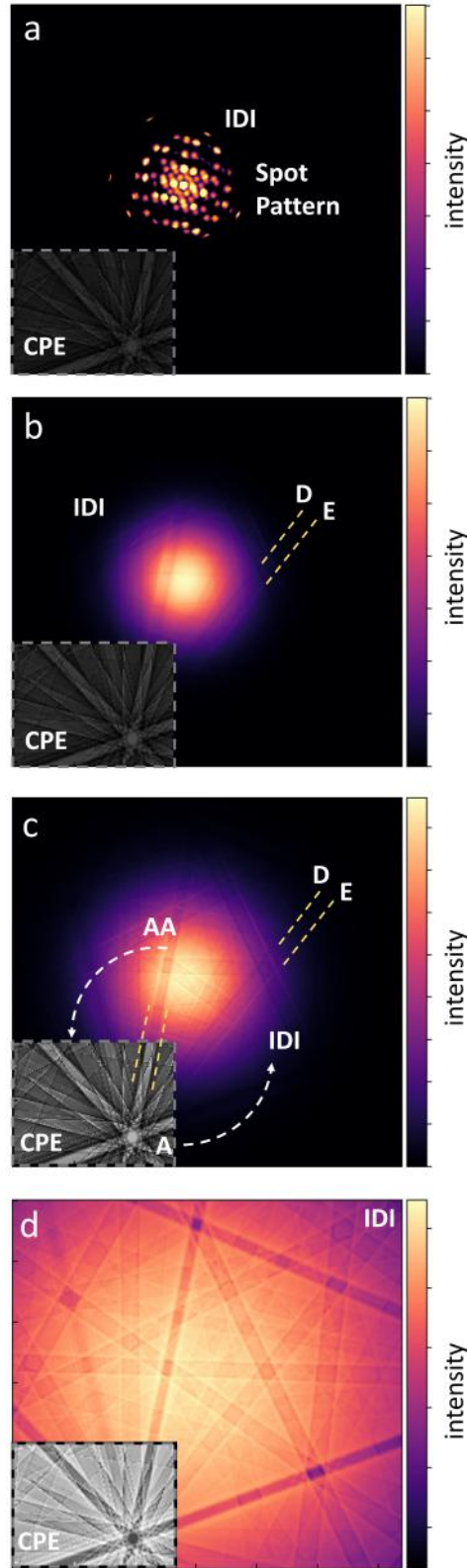


**Figure 11:** Qualitative thickness dependence of Kikuchi diffraction features, using the geometry for the Mg example pattern of Fig.7 from Brodu *et al.* [66]: (a) very thin sample with diffraction spots, at larger scattering angles there is a CPE pattern with low intensity (inset); (b) low thickness with strongly overlapping diffraction orders, E/D effects due to the intensity gradient across a band profile, anomalous absorption is low, the CPE pattern has increased intensity (inset); (c) increased thickness with significant anomalous absorption causing dark Kikuchi bands in the IDI intensity; the CPE pattern with higher-intensity bands increases in relative intensity from a-c, i.e. there is a competition with the IDI intensity of opposite contrast, causing possible band contrast reversals between outer and inner regions of the pattern; (d) very thick sample, reduced E/D effects due to reduced intensity gradients, anomalous absorption is dominating both the CPE and IDI contributions showing dark Kikuchi bands.

In Figure 11c, absorption effects have become increasingly important with a larger sample thickness. Anomalous absorption creates the appearance of dark Kikuchi bands, which however are still "floating" on a relatively high background as compared to the outer areas of the pattern. The dark areas at larger scattering angles relative to the incident beam (and between the diffraction spots) would be completely void of intensity for perfect coherent scattering of a single plane-wave beam. However, intensity is scattered towards these regions by inelastic and incoherent processes, which are usually considered as an absorption from the coherent wave field. The appearance of the CPE pattern is caused by the same anomalous "absorption" effects which cause the loss of intensity from the coherently scattered portion of an incident beam. Our model can thus treat the effect that the "absorbed" electrons actually do not disappear from the experiment, but contribute a CPE pattern in the low-intensity areas. This is why we have symbolized in Figure 11c that there is an interplay between anomalous absorption (AA) which can provide large scattering angles to redistribute intensity to all angles, and the creation of IDI distribution, which evolves with thickness due to the momentum broadening by multiple scattering effects in a sample [124] and the concomitant loss of coherence which diminishes the CPE contribution due to the dominating "normal" absorption (A) e.g. by plasmon creation (which does not vary in the unit cell and thus cannot create a new CPE pattern after the inelastic event). The specific weighting of the different contrast effects in different regions of the pattern is not predicted by our phenomenological model. The related contrast reversal effects could be described, for example, by effective parameters which change depending on the direction in the pattern.

In Figure 11d, we show the limiting situation of a thick sample which is dominated by anomalous absorption effects. Any remaining E/D features are diminished due to the reduced gradients of intensity. Based on the same anomalous absorption effects, also the CPE pattern will show reduced and inverted contrast for thick samples, as seen in the inset in Figure 11d.

In the general experimental situation of EBSD, which usually does not involve any specific filtering by electron energy analyzers etc, all the effects shown in Figure 11 can be present simultaneously in a single Kikuchi diffraction pattern. Comparison to Figure 2 shows that Figure 11a and b relate to the experimental situation in Figure 2a, while Figure 11b corresponds to the excess-deficiency effects seen in Figure 2b. Figure 11c describes the dark Kikuchi bands dominating a thick sample in Figure 2c.

It is important to note that image processing techniques can strongly modify the relative contrast of features, and thus obscure the different origin of the contrast mechanism. For example, image processing can make it impossible to recognize that the "dark" Kikuchi bands with inverted contrast in the high intensity region in the center of Figure 11(c) initially had a higher absolute intensity than the low-intensity "light" CPE bands in the outer region of Figure 11(d). Such large changes between the experimental raw patterns and the resulting processed images after background processing are discussed, for example, in Brodu *et al.* [66], Figure 9, for different thicknesses of single-crystalline silicon.

For an illustration of the severe effects of Kikuchi pattern image processing, we show in Figure 12 a comparison of raw and processed on-axis TKD patterns for a thin sample of Mg ( $d = 180 \pm 20$  nm,  $E = 20$  keV) which was also studied in [66]. The raw pattern in Figure 12(a) shows high intensity near the on-axis transmitted beam features, with diffraction spots and a dominating IDI excess-deficiency Kikuchi line contrast due to the intensity gradient (relevant for on-axis TKD and also for selected aread diffraction in the TEM). While the intensity is strongly decreasing for increasing scattering angles in the raw pattern, the processed pattern in Figure 12(b) allows to see the low-intensity CPE contrast which is dominating at these larger scattering angles (i.e. relevant for conventional EBSD, off-axis TKD, and high-angle dark field imaging in the TEM). The general Kikuchi contrast always comprises contributions from both IDI and CPE contrast. The dashed circle is shown to indicate which type of contrast is dominating in the different pattern areas. The viewing angle of the pattern shown in Figure 12 covers about 50 degrees in both dimensions, and we can roughly estimate that scattering angles

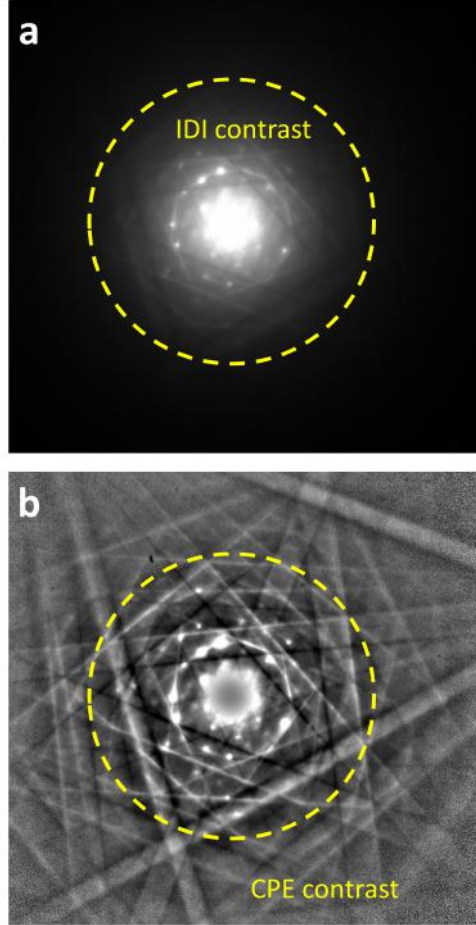


**Figure 12:** Mixing of different contrast contributions in on-axis transmission Kikuchi diffraction for a thin sample of Mg ( $d = 180 \pm 20$  nm,  $E = 20$  keV ) [66]: (a) raw pattern showing high intensity near the on-axis transmitted beam features, with dominating IDI contrast due to the intensity gradient (relevant for on-axis TKD) (b) pattern processed to show the low-intensity CPE contrast which is dominating at larger scattering angles (i.e. relevant for conventional EBSD or off-axis TKD).



larger than about 10 to 15 degrees from the incident beam are dominated by CPE contrast for the the studied sample. Note how in Figure12, the Bragg-lines provide a common, continuous geometrical framework for various, scattering-angle-dependent, contrast contributions, which combine to form the observed Kikuchi band contrast features. The Kikuchi bands are formed by “filling in” of intensity on the common geometrical framework of Bragg lines, depending on various different, scattering-angle-dependent, contrast contributions, i.e. in general there is no single constant mechanism that dominates any individual Kikuchi band, and we cannot speak of a Kikuchi band independent of the scattering conditions.

We can summarize that the physical basis of our phenomenological model is consistent with the general experimental observations described in [70], which describes the transitions as shown in Figure11a to d. As already indicated by Figure11a, the simulation model for the IDI distribution also includes as the limiting case some of the effects which are relevant for TEM-like spot diffraction or CBED patterns by defining suitable incoherent incident beam intensity distributions which would generalize the specific equations 19 and 20 chosen in the present study. In turn, the CPE part of the present simulation model is relevant for describing the Kikuchi effects of TEM and CBED patterns.

Concerning theoretical pattern simulations, it is the large-angle scattering geometry of EBSD which benefits from the simplifications introduced by the dominating coherent point emitter model. In a first approximation, the interpretation of large-angle scattering Kikuchi patterns is possible even by completely neglecting the excess-deficiency effects. As was indicated by the systematic influence on the projection center fits discussed above, high-precision pattern matching applications, however, have to take into account the additional excess-deficiency contributions which are neglected by a CPE model.

## 5. Summary & Conclusions

We have discussed a refined simulation model which includes the Kikuchi diffraction effects of an incoherent diffuse electron intensity distribution. The model treats the formation of excess-deficiency features based on gradients in an incoherent background intensity.

The improved agreement between experimentally measured Kikuchi diffraction patterns and simulated patterns was shown for example Kikuchi patterns measured in a conventional backscattering geometry of EBSD, as well as for TKD patterns measured in an on-axis transmission geometry.

In the analyzed example patterns, the simulations indicated that the relatively pronounced excess-deficiency features provide a signal contribution of about 10%. We derived a phenomenological correction model based on the analytical two-beam approximation of dynamical electron diffraction. The comparison to the many-beam Thomas-Humphreys model indicated that the two-beam model can be a practical solution for including the excess-deficiency effects in pattern matching applications, taking into account that the analytical formulas can be efficiently implemented on GPUs.

As an application of the refined simulation model, we have discussed the possible magnitudes of systematic changes in the calibration of the experimental geometry, which we found to be in the order of  $10^{-3}$  to  $10^{-2}$ . These values can result in similar changes of absolute lattice parameters and strain when these are determined based on simulations that neglect E/D effect. Results of some recent numerical simulation studies concerning a potentially very high precision projection center and strain determination [14, 30, 125] are thus difficult to transfer directly to a correspondingly high precision in realistic experimental situations since excess-deficiency effects have not been accounted for in the underlying theoretical model of these studies. Optical distortions will be an additional source of error that would need to be treated in high-resolution pattern matching studies [126]. Concerning EBSD-based lattice parameter measurements, it is not unreasonable to expect that it will be hard to surpass current limits which have been

achieved under much better controlled conditions in the TEM, where minimum errors in the range of  $\times 10^{-4}$  to  $\times 10^{-3}$  have been estimated [127–133].

We have seen that the appearance of excess-deficiency features leads to intensity asymmetries in experimental Kikuchi diffraction patterns which are mainly governed by the asymmetry of the experimental setup, and not by any asymmetries of the observed crystal structure. The recently proposed automated detection of space groups from experimental Kikuchi patterns using machine learning approaches [134, 135] relies on the assumed ability to discriminate the specific *asymmetries* between possible crystal structures based on correspondingly specific *asymmetries* in Kikuchi patterns [136]. This approach is limited by Neumann’s principle, which implies that asymmetries of a crystal structure do not necessarily also result in an asymmetric physical property, and thus a Kikuchi pattern can be more symmetric than the crystal structure. On the other hand, the unspecific nature of excess-deficiency effects with respect to crystal structure asymmetries is a parasitic effect that creates a Kikuchi diffraction pattern of lower symmetry than the crystal structure, which needs to be taken into account in applications of machine learning models for automated space group detection by EBSD.

As we have discussed in Section 4.3, and shown in Figure 11, a number of details of Kikuchi pattern formation process can be described by assuming suitable phenomenological parameters in our refined simulation model. The complexity of Kikuchi diffraction effects in a general experimental pattern is seen by the principal need to include the weighted, thickness- and energy-dependent contributions of the effects shown in Figure 11. While our phenomenological approach treats the thickness-dependent competition of various coherent and incoherent electron scattering effects only by a severely restricted average model [137], it is expected to deliver improved Kikuchi diffraction pattern simulations which can be used to extract more accurate crystallographic information from experimental datasets.

## Acknowledgements

We thank E. Bouzy and E. Brodu for providing raw data of the TKD measurements discussed in [66]. This work has been supported by the Polish National Agency for Academic Exchange (NAWA) grants no. PPN/ULM/2019/1/00068/U/00001 and by Polish National Science Centre (NCN) grant no. 2020/37/B/ST5/03669. The authors acknowledge the ARCHIE-WeSt High Performance Computer ([www.archie-west.ac.uk](http://www.archie-west.ac.uk)) based at the University of Strathclyde, as well as grant EP/P015719/1 for computer resources.

## References

- [1] A. J. Schwartz, M. Kumar, B. L. Adams (Eds.), *Electron Backscatter Diffraction in Materials Science*, Kluwer Academic / Plenum Publications, New York, 2000.
- [2] A. Winkelmann, C. Trager-Cowan, F. Sweeney, A. P. Day, P. Parbrook, Many-beam dynamical simulation of electron backscatter diffraction patterns, *Ultramicroscopy* 107 (4-5) (2007) 414–21. doi:10.1016/j.ultramic.2006.10.006.
- [3] A. Winkelmann, Dynamical Simulation of Electron Backscatter Diffraction Patterns, in: A. J. Schwartz, M. Kumar, B. L. Adams, D. P. Field (Eds.), *Electron Backscatter Diffraction in Materials Science*, Springer, Berlin, 2009, Ch. 2, pp. 21–3. doi:10.1007/978-0-387-88136-2\_2. URL [http://www.springer.com/cda/content/document/cda\\_downloaddocument/9780387881355-c2.pdf?SGWID=0-0-45-749108-p173906909](http://www.springer.com/cda/content/document/cda_downloaddocument/9780387881355-c2.pdf?SGWID=0-0-45-749108-p173906909)
- [4] C. Maurice, K. Dzieciol, R. Fortunier, A method for accurate localisation of EBSD pattern centres, *Ultramicroscopy* 111 (2) (2011) 140–148. doi:10.1016/j.ultramic.2010.10.007.
- [5] P. G. Callahan, M. De Graef, Dynamical Electron Backscatter Diffraction Patterns. Part I: Pattern Simulations, *Microscopy and Microanalysis* 19 (2013) 1255–1265. doi:10.1017/S1431927613001840.
- [6] A. Winkelmann, G. Nolze, M. Vos, F. Salvat-Pujol, W. S. M. Werner, Physics-based simulation models for EBSD: advances and challenges, *IOP Conference Series: Materials Science and Engineering* 109 (1) (2016) 012018. doi:10.1088/1757-899X/109/1/012018.
- [7] G. Nolze, C. Grosse, A. Winkelmann, Kikuchi pattern analysis of noncentrosymmetric crystals, *Journal of Applied Crystallography* 48 (5) (2015) 1405–1419. doi:10.1107/s1600576715014016.
- [8] A. Winkelmann, G. Nolze, Point-group sensitive orientation mapping of non-centrosymmetric crystals, *Appl. Phys. Lett.* 106 (7) (2015) 072101. doi:10.1063/1.4907938.
- [9] A. Winkelmann, G. Nolze, Chirality determination of quartz crystals using Electron Backscatter Diffraction, *Ultramicroscopy* 149 (2015) 58–63. doi:10.1016/j.ultramic.2014.11.013.
- [10] U. Burkhardt, H. Borrmann, P. Moll, M. Schmidt, Y. Grin, A. Winkelmann, Absolute structure from scanning electron microscopy, *Scientific Reports* 10 (2020) 4065. doi:10.1038/s41598-020-59854-y.
- [11] A. Winkelmann, G. Cios, T. Tokarski, P. Bała, Y. Grin, U. Burkhardt, Fixing Left and Right: Assignment of Chiral Elemental Crystal Structures using Kikuchi Diffraction, arXiv (2011.14422) (Yesvember 2020). arXiv:2011.14422.
- [12] U. Burkhardt, A. Winkelmann, H. Borrmann, A. Dumitriu, M. König, G. Cios, Y. Grin, Assignment of enantiomorphs for the chiral allotrope  $\beta$ -Mn by diffraction methods, *Science Advances* 7 (20) (2021) eabg0868. doi:10.1126/sciadv.abg0868.
- [13] M. J. Burch, C. M. Fancher, S. Patala, M. De Graef, E. C. Dickey, Mapping 180° polar domains using electron backscatter diffraction and dynamical scattering simulations, *Ultramicroscopy* 173 (2017) 47–51. doi:10.1016/j.ultramic.2016.11.013.
- [14] E. L. Pang, P. M. Larsen, C. A. Schuh, Resolving pseudosymmetry in tetragonal ZrO<sub>2</sub> using electron backscatter diffraction with a modified dictionary indexing approach, *Journal of Applied Crystallography* 53 (4) (jul 2020). doi:10.1107/s160057672000864x.
- [15] G. Nolze, A. Winkelmann, About the reliability of EBSD measurements: Data enhancement, *IOP Conference Series: Materials Science and Engineering* 891 (2020) 012018. doi:10.1088/1757-899X/891/1/012018.



- [16] F. Ram, M. De Graef, Phase differentiation by electron backscatter diffraction using the dictionary indexing approach, *Acta Materialia* 144 (2018) 352–364. doi:10.1016/j.actamat.2017.10.069.
- [17] T. Friedrich, A. Bochmann, J. Dinger, S. Teichert, Application of the pattern matching approach for EBSD calibration and orientation mapping, utilising dynamical EBSP simulations, *Ultramicroscopy* 184 (2018) 44–51. doi:10.1016/j.ultramic.2017.10.006.
- [18] T. Tanaka, A. J. Wilkinson, Pattern matching analysis of electron backscatter diffraction patterns for pattern centre, crystal orientation and absolute elastic strain determination – accuracy and precision assessment, *Ultramicroscopy* 202 (2019) 87–99. doi:10.1016/j.ultramic.2019.04.006.
- [19] E. L. Pang, P. M. Larsen, C. A. Schuh, Global optimization for accurate determination of EBSD pattern centers, *Ultramicroscopy* 209 (2020) 112876. doi:10.1016/j.ultramic.2019.112876.
- [20] A. Winkelmann, G. Nolze, G. Cios, T. Tokarski, P. Bala, Refined calibration model for improving the orientation precision of electron backscatter diffraction maps, *Materials* 13 (12) (2020) 2816. doi:10.3390/ma13122816.
- [21] G. Nolze, A. Winkelmann, A. P. Boyle, Pattern matching approach to pseudosymmetry problems in electron backscatter diffraction, *Ultramicroscopy* 160 (2016) 146–154. doi:10.1016/j.ultramic.2015.10.010.
- [22] S. Singh, F. Ram, M. De Graef, Application of forward models to crystal orientation refinement, *Journal of Applied Crystallography* 50 (6) (2017) 1664–1676. doi:10.1107/s1600576717014200.
- [23] K. Marquardt, M. D. Graef, S. Singh, H. Marquardt, A. Rosenthal, S. Koizumi, Quantitative electron backscatter diffraction (EBSD) data analyses using the dictionary indexing (DI) approach: Overcoming indexing difficulties on geological materials, *American Mineralogist* 102 (9) (2017) 1843–1855. doi:10.2138/am-2017-6062.
- [24] G. Nolze, M. Jürgens, J. Olbricht, A. Winkelmann, Improving the precision of orientation measurements from technical materials via EBSD pattern matching, *Acta Materialia* 159 (2018) 408–415. doi:10.1016/j.actamat.2018.08.028.
- [25] A. Winkelmann, B. M. Jablon, V. S. Tong, C. Trager-Cowan, K. P. Mingard, Improving EBSD precision by orientation refinement with full pattern matching, *Journal of Microscopy* 277 (2) (2020) 79–92. doi:10.1111/jmi.12870.
- [26] G. Sparks, P. A. Shade, M. D. Uchic, S. R. Niezgoda, M. J. Mills, M. Obstalecki, High-precision orientation mapping from spherical harmonic transform indexing of electron backscatter diffraction patterns, *Ultramicroscopy* (2021) 113187. doi:10.1016/j.ultramic.2020.113187.
- [27] G. Nolze, A. Winkelmann, G. Cios, T. Tokarski, Tetragonality mapping of martensite in a high-carbon steel by EBSD, *Materials Characterization* 175 (2021) 111040. doi:10.1016/j.matchar.2021.111040.
- [28] T. Tanaka, A. J. Wilkinson, High Angular Resolution Electron Backscatter Diffraction Studies of Tetragonality in Fe-C Martensitic Steels, *Microscopy and Microanalysis* 24 (S1) (2018) 962–963. doi:10.1017/s1431927618005305.
- [29] A. Winkelmann, G. Nolze, G. Cios, T. Tokarski, Mapping of local lattice parameter ratios by projective Kikuchi pattern matching, *Physical Review Materials* 2 (2018) 123803. doi:10.1103/PhysRevMaterials.2.123803.
- [30] C. Kurniawan, C. Zhu, M. De Graef, Deformation state extraction from electron backscatter diffraction patterns via simulation-based pattern-matching, *Scripta Materialia* 190 (2021) 147–152. doi:10.1016/j.scriptamat.2020.09.004.
- [31] T. Tanaka, N. Maruyama, N. Nakamura, A. J. Wilkinson, Tetragonality of Fe-C martensite - a pattern matching electron backscatter diffraction analysis compared to X-ray diffraction, *Acta Materialia* 195 (2020) 728–738. doi:10.1016/j.actamat.2020.06.017.
- [32] C. Zhu, M. De Graef, EBSD pattern simulations for an interaction volume containing lattice defects, *Ultramicroscopy* (2020) 113088. doi:10.1016/j.ultramic.2020.113088.
- [33] Y. H. Chen, S. U. Park, D. Wei, G. Newstadt, M. A. Jackson, J. P. Simmons, M. De Graef, A. O. Hero, A dictionary approach to electron backscatter diffraction indexing, *Microscopy and Microanalysis* 21 (03) (2015) 739–752. doi:10.1017/s1431927615000756.
- [34] A. Foden, D. M. Collins, A. J. Wilkinson, T. B. Britton, Indexing electron backscatter diffraction patterns with a refined template matching approach, *Microscopy and Microanalysis* 25 (S2) (2019) 1962–1963. doi:10.1017/s1431927619010547.
- [35] R. Hielscher, F. Bartel, T. B. Britton, Gazing at crystal balls: Electron backscatter diffraction pattern analysis and cross correlation on the sphere, *Ultramicroscopy* 207 (2019) 112836. doi:10.1016/j.ultramic.2019.112836.
- [36] W. C. Lenthe, S. Singh, M. De Graef, A spherical harmonic transform approach to the indexing of electron back-scattered diffraction patterns, *Ultramicroscopy* 207 (2019) 112841. doi:10.1016/j.ultramic.2019.112841.
- [37] Z. Ding, E. Pascal, M. De Graef, Indexing of electron back-scatter diffraction patterns using a convolutional neural network, *Acta Materialia* 199 (2020) 370–382. doi:10.1016/j.actamat.2020.08.046.
- [38] R. Høier, Multiple scattering and dynamical effects in diffuse electron scattering, *Acta Cryst. A* 29 (1973) 663–672. doi:10.1107/S0567739473001671.
- [39] C. J. Rossouw, L. A. Bursill, Interpretation of Dynamical Diffuse Scattering of Fast Electrons in Rutile, *Acta Cryst. A* 41 (1985) 320–327. doi:10.1107/S0108767385000708.
- [40] K. Marthinsen, R. Høier, On the breakdown of Friedel's law in electron backscattered channelling patterns, *Acta Cryst. A* 44 (5) (1988) 700–707. doi:10.1107/S0108767388004532.
- [41] C. J. Rossouw, P. R. Miller, T. W. Josefsson, L. J. Allen, Zone-axis back-scattered electron contrast for fast electrons, *Philosophical Magazine A* 70 (January) (1994) 985–998. doi:10.1080/01418619408242944.
- [42] A. Winkelmann, T. B. Britton, G. Nolze, Constraints on the effective electron energy spectrum in backscatter Kikuchi diffraction, *Physical Review B* 99 (2019) 064115. doi:10.1103/PhysRevB.99.064115.
- [43] B. G. Mendis, Theory underpinning multislice simulations with plasmon energy losses, *Microscopy* 69 (3) (2020) 173–175. doi:10.1093/jmicro/dfaa003.
- [44] B. G. Mendis, J. Barthel, S. D. Findlay, L. J. Allen, Inelastic scattering in electron backscatter diffraction and electron channeling contrast imaging, *Microscopy and Microanalysis* (2020) 1–11. doi:10.1017/s1431927620024605.
- [45] L. Cheng, Y. Ming, Z. J. Ding, Bohmian trajectory-Bloch wave approach to dynamical simulation of electron diffraction in crystal, *New Journal of Physics* (2018). doi:10.1088/1367-2630/aae8f1.
- [46] S. Rudinsky, R. Gauvin, A hydrodynamic approach to electron beam imaging using a Bloch wave representation, *Ultramicroscopy* 212 (2020) 112979. doi:10.1016/j.ultramic.2020.112979.
- [47] Q. B. Liu, C. Y. Cai, G. W. Zhou, Y. G. Wang, Comparison of EBSD patterns simulated by two multislice methods, *Journal of Microscopy* 264 (1) (2016) 71–78. doi:10.1111/jmi.12418.
- [48] M. N. Alam, M. Blackman, D. W. Pashley, High-Angle Kikuchi Patterns, *Proc. Royal Soc. A* 221 (1145) (1954) 224–242. doi:10.1098/rspa.1954.0017.
- [49] Y. Kainuma, The theory of Kikuchi patterns, *Acta Cryst.* 8 (1955) 247. doi:10.1107/S0365110X55000832.
- [50] R. Uyeda, M. Nonoyama, The Observation of Thick Specimens by High Voltage Electron Microscopy. Experiment with Molybdenite Films at 50–500 kV, *Jpn. J. Appl. Phys.* 6 (5) (1967) 557–566. doi:10.1143/JJAP.6.557.
- [51] R. Uyeda, M. Nonoyama, The Observation of Thick Specimens by High Voltage Electron Microscopy. {II.} Experiment with Molybdenite Films at 50–1200 kV., *Jpn. J. Appl. Phys.* 7 (3) (1968) 200–208. doi:10.1143/JJAP.7.200.
- [52] R. Uyeda, Dynamical effects in high-voltage electron diffraction, *Acta Cryst. A* 24 (1968) 175–181. doi:10.1107/S0567739468000240.
- [53] G. Thomas, Kikuchi Electron Diffraction and Applications, in: S. Amelinckx, R. Gevers, G. Remaut, J. Van Landuyt (Eds.), *Modern Diffraction and Imaging Techniques in Materials Science*, North-Holland, 1970, pp. 159–185. URL <https://www.worldcat.org/isbn/0444100288>
- [54] G. R. Booker, Scanning Electron Microscopy: Electron Channeling Effects, in: S. Amelinckx, R. Gevers, G. Remaut, J. Van Landuyt (Eds.), *Modern Diffraction and Imaging Techniques in Materials Science*, North-Holland, 1970, pp. 613–653. URL <https://www.worldcat.org/isbn/0444100288>
- [55] L. E. Thomas, C. J. Humphreys, Kikuchi patterns in a high voltage electron microscope, *Physica Status Solidi (a)* 3 (3) (1970) 599–615. doi:10.1002/pssa.1970003036.
- [56] D. J. Dingley, K. Z. Baba-Kishi, V. Randle, Atlas of backscattering Kikuchi diffraction patterns, *Inst. of Physics Publ.*, 1995.
- [57] A. Winkelmann, Dynamical effects of anisotropic inelastic scattering in electron backscatter diffraction, *Ultramicroscopy* 108 (2008) 1546–1550. doi:10.1016/j.ultramic.2008.05.002.
- [58] R. H. Geiss, R. R. Keller, D. T. Read, Transmission Electron Diffraction From Nanoparticles, Nanowires and Thin Films in an SEM With Conventional EBSP Equipment, *Microscopy and Microanalysis* 16 (S2) (2010) 1742–1743. doi:10.1017/s1431927610062227.
- [59] R. H. Geiss, R. Keller, S. Sitzman, P. Rice, New Method of Transmission Electron Diffraction to Characterize Nanomaterials in the SEM, *Microscopy and Microanalysis* 17 (S2) (2011) 386–387. doi:10.1017/s1431927611002807.
- [60] R. R. Keller, R. H. Geiss, Transmission EBSD from 10 nm domains in a scanning electron microscope., *J. Microsc.* 245 (3) (2012) 245–51. doi:10.1111/j.1365-2818.2011.03566.x.
- [61] P. W. Trimby, Orientation mapping of nanostructured materials using transmission Kikuchi diffraction in the scanning electron microscope., *Ultramicroscopy* 120 (2012) 16–24. doi:10.1016/j.ultramic.2012.06.004. URL <http://www.sciencedirect.com/science/article/pii/S0304399112001258>
- [62] N. Brodusch, H. Demers, R. Gauvin, Nanometres-resolution Kikuchi patterns from materials science specimens with transmission electron forward scatter diffraction in the scanning electron microscope, *J. Microsc.* 250 (June 2012) (2013) 1–14. doi:10.1111/jmi.12007.
- [63] K. P. Rice, R. R. Keller, M. P. Stoykovich, Specimen-thickness effects on transmission Kikuchi patterns in the scanning electron microscope, *Journal of Microscopy* 254 (3) (2014) 129–136. doi:10.1111/jmi.12124.
- [64] G. C. Sneddon, P. W. Trimby, J. M. Cairney, Transmission Kikuchi diffraction in a scanning electron microscope: A Review, *Materials Science and Engineering: R: Reports* 110 (2016) 1–12. doi:10.1016/j.mser.2016.10.001. URL <http://www.sciencedirect.com/science/article/pii/S0927796X16300493>

- [65] J. J. Fundenberger, E. Bouzy, D. Goran, J. Guyon, H. Yuan, A. Morawiec, Orientation mapping by transmission-SEM with an on-axis detector, *Ultramicroscopy* 161 (2016) 17–22. doi:10.1016/j.ultramic.2015.11.002.
- [66] E. Brodu, E. Bouzy, J.-J. Fundenberger, Diffraction contrast dependence on sample thickness and incident energy in on-axis Transmission Kikuchi Diffraction in SEM, *Ultramicroscopy* 181 (2017) 123–133. doi:10.1016/j.ultramic.2017.04.017.
- [67] H. Yuan, E. Brodu, C. Chen, E. Bouzy, J.-J. Fundenberger, L. S. Toth, On-axis versus off-axis Transmission Kikuchi Diffraction technique: application to the characterisation of severe plastic deformation-induced ultrafine-grained microstructures, *Journal of Microscopy* 267 (1) (2017) 70–80. doi:10.1111/jmi.12548.
- [68] F. Niessen, A. Burrows, A. Bastos da Silva Fanta, A systematic comparison of on-axis and off-axis transmission Kikuchi diffraction, *Ultramicroscopy* 186 (2018) 158–170. doi:10.1016/j.ultramic.2017.12.017.
- [69] N. Brodusch, H. Demers, R. Gauvin, Imaging with a Commercial Electron Backscatter Diffraction (EBSD) Camera in a Scanning Electron Microscope: A Review, *Journal of Imaging* 4 (7) (2018) 88. doi:10.3390/jimaging4070088.
- [70] L. Reimer, Electron diffraction methods in TEM, STEM and SEM, *Scanning* 2 (1) (1979) 3–19. doi:10.1002/sca.4950020101.
- [71] L. E. Thomas, Kikuchi patterns in high voltage electron microscopy, *Philosophical Magazine* 26 (6) (1972) 1447–1465. doi:10.1080/14786437208220355.
- [72] F. N. Chukhovskii, L. A. Alexanjan, Z. G. Pinsker, Dynamical Treatment of Kikuchi Patterns, *Acta Cryst. A* 29 (1973) 38. doi:10.1107/S0567739473000094.
- [73] Q. Shi, D. Loisonard, C. Dan, F. Zhang, H. Zhong, H. Li, Y. Li, Z. Chen, H. Wang, S. Roux, Calibration of crystal orientation and pattern center of EBSD using integrated digital image correlation, *Materials Characterization* 178 (2021) 111206. doi:10.1016/j.matchar.2021.111206.
- [74] P. R. Buseck, J. M. Cowley, L. Eyring (Eds.), *High-resolution transmission electron microscopy and associated techniques*, Oxford University Press, New York, 1988.
- [75] Z. L. Wang, *Elastic and Inelastic Scattering in Electron Diffraction and Imaging*, Springer US, 1995. doi:10.1007/978-1-4899-1579-5.
- [76] P. Schattschneider, M. Nelhiebel, M. Souchay, B. Jouffrey, The physical significance of the mixed dynamic form factor, *Micron* 31 (2000) 333–345. doi:10.1016/S0968-4328(99)00112-2.
- [77] J. M. Cowley, J. K. Gjønnes, Diffuse scattering in electron diffraction, in: *International Tables for Crystallography*, International Union of Crystallography, 2010, pp. 540–546. doi:10.1107/97809553602060000775.
- [78] J. M. Zuo, J. C. H. Spence, Diffuse Scattering, in: *Advanced Transmission Electron Microscopy*, Springer New York, 2017, pp. 403–440. doi:10.1007/978-1-4939-6607-3\_13.
- [79] J. Gjønnes, The influence of Bragg scattering on inelastic and other forms of diffuse scattering of electrons, *Acta Crystallographica* 20 (2) (1966) 240–249. doi:10.1107/s0365110x66000471.
- [80] K. Ishida, Inelastic Scattering of Fast Electrons by Crystals. II. The Excess and Defect Kikuchi Bands, *Journal of the Physical Society of Japan* 30 (5) (1971) 1439–1448. doi:10.1143/jpsj.30.1439.
- [81] T. Kawamura, Absorption Effect and Contrast Change of Kikuchi Lines in Reflection Patterns, *Physica Status Solidi (a)* 27 (2) (1975) 591–598. doi:10.1002/pssa.2210270230.
- [82] P. Rez, C. J. Humphreys, M. J. Whelan, The distribution of intensity in electron diffraction patterns due to phonon scattering, *Philosophical Magazine* 35 (1) (1977) 81–96. doi:10.1080/14786437708235974.
- [83] A. Siems, Quantitative Untersuchungen an Kikuchi-Strukturen. I. Energieanalyse von Intensitätsprofilen, *Physica Status Solidi (a)* 49 (2) (1978) 621–628. doi:10.1002/pssa.2210490225.
- [84] A. Siems, Quantitative Untersuchungen an Kikuchi-Strukturen. II. Thermisch diffuse Streuung, *Physica Status Solidi (a)* 56 (2) (1979) 697–709. doi:10.1002/pssa.2210560237.
- [85] C. J. Rossouw, Coherence in inelastic electron scattering, *Ultramicroscopy* 16 (1985) 241. doi:10.1016/0304-3991(85)90078-6.
- [86] D. M. Bird, A. G. Wright, Phase dependence of Kikuchi patterns. I. Theory, *Acta Crystallographica Section A Foundations of Crystallography* 45 (1) (1989) 104–109. doi:10.1107/s0108767388009304.
- [87] L. Reimer, U. Heilers, G. Saliger, Kikuchi band contrast in diffraction patterns recorded by transmitted and backscattered electrons, *Scanning* 8 (3) (1986) 101–118. doi:10.1002/sca.4950080303.
- [88] J. Mayer, C. Deiningger, L. Reimer, Electron spectroscopic diffraction, in: L. Reimer (Ed.), *Energy-Filtering Transmission Electron Microscopy*, Springer Berlin Heidelberg, Berlin, Heidelberg, 1995, pp. 291–345. doi:10.1007/978-3-540-48995-5\_6.
- [89] D. B. Williams, C. B. Carter, Kikuchi Diffraction, in: *Transmission Electron Microscopy*, Springer US, 2009, pp. 311–322. doi:10.1007/978-0-387-76501-3\_19.
- [90] S. Suzuki, Features of Transmission EBSD and its Application, *JOM* 65 (2013) 1254–1263. doi:10.1007/s11837-013-0700-6.
- [91] J.-W. Shih, K.-W. Kuo, J.-C. Kuo, T.-Y. Kuo, Effects of accelerating voltage and specimen thickness on the spatial resolution of transmission electron backscatter diffraction in Cu, *Ultramicroscopy* 177 (2017) 43–52. doi:10.1016/j.ultramic.2017.01.020.
- [92] A. Deal, T. Hooghan, A. Eades, Energy-filtered electron backscatter diffraction, *Ultramicroscopy* 108 (2008) 116–125. doi:10.1016/j.ultramic.2007.03.010.
- [93] A. Winkelmann, K. Aizel, M. Vos, Electron energy loss and diffraction of backscattered electrons from silicon, *New Journal of Physics* 12 (2010) 053001. doi:10.1088/1367-2630/12/5/053001.
- [94] M. Vos, A. Winkelmann, Effects of multiple elastic and inelastic scattering on energy-resolved contrast in Kikuchi diffraction, *New Journal of Physics* 21 (12) (2019) 123018. doi:10.1088/1367-2630/ab5cd1.
- [95] A. Winkelmann, G. Nolze, S. Vespucchi, G. Naresh-Kumar, C. Trager-Cowan, A. Vilalta-Clemente, A. J. Wilkinson, M. Vos, Diffraction effects and inelastic electron transport in angle-resolved microscopic imaging applications, *Journal of Microscopy* 267 (2017) 330–346. doi:10.1111/jmi.12571.
- [96] J. M. Cowley, *Diffraction Physics*, 3rd Edition, North-Holland, Amsterdam, 1995.
- [97] D. B. Williams, C. B. Carter, *Transmission Electron Microscopy*, 2nd Edition, Springer Science + Business Media, 2009. doi:10.1007/978-0-387-76501-3. URL <http://dx.doi.org/10.1007/978-0-387-76501-3>
- [98] J. P. Morniroli, *Large-Angle Convergent-Beam Electron Diffraction*, CRC Press, Boca Raton, 2004.
- [99] S. Zaefferer, On the formation mechanisms, spatial resolution and intensity of backscatter Kikuchi patterns, *Ultramicroscopy* 107 (2-3) (2007) 254–66. doi:10.1016/j.ultramic.2006.08.007.
- [100] A. Winkelmann, Model mechanisms in Kikuchi pattern formation from crystals, *Crystal Research and Technology* 52 (4) (2017) 1600288. doi:10.1002/crat.201600288.
- [101] H. Kohl, H. Rose, Theory of Image Formation by Inelastically Scattered Electrons in the Electron Microscope, in: *Advances in Electronics and Electron Physics*, Elsevier, 1985, pp. 173–227. doi:10.1016/s0065-2539(08)60878-1.
- [102] P. Schattschneider, W. S. M. Werner, Coherence in electron energy loss spectrometry, *Journal of Electron Spectroscopy and Related Phenomena* 143 (2-3) (2005) 81–95. doi:10.1016/j.elspec.2004.09.029.
- [103] A. Winkelmann, M. Vos, Site-Specific Recoil Diffraction of Backscattered Electrons in Crystals, *Phys. Rev. Lett.* 106 (8) (2011) 085503. doi:10.1103/PhysRevLett.106.085503.
- [104] A. Winkelmann, M. Vos, The role of localized recoil in the formation of Kikuchi patterns., *Ultramicroscopy* 125 (2013) 66–71. doi:10.1016/j.ultramic.2012.11.001.
- [105] O. Fedchenko, A. Winkelmann, S. Chernov, K. Medjanik, S. Babenkov, S. Y. Agustsson, D. Vasilyev, M. Hoesch, H.-J. Elmers, G. Schönhense, Emitter-site specificity of hard x-ray photoelectron kikuchi-diffraction, *New Journal of Physics* 22 (10) (2020) 103002. doi:10.1088/1367-2630/abb68b.
- [106] F. Fujimoto, G. Lehmpfuhl, Contrast of Kossel Patterns in Electron Diffraction, *Zeitschrift für Naturforschung A* 29 (12) (1974) 1929–1930b. doi:10.1515/zna-1974-1238.
- [107] H. Hashimoto, A. Howie, M. J. Whelan, Anomalous electron absorption effects in metal foils: theory and comparison with experiment, *Proceedings of the Royal Society of London. Series A. Mathematical and Physical Sciences* 269 (1336) (1962) 80–103. doi:10.1098/rspa.1962.0164.
- [108] L. Reimer, H. Kohl, *Transmission Electron Microscopy*, 5th Edition, Springer, 2008. doi:10.1007/978-0-387-40093-8.
- [109] A. Winkelmann, G. Nolze, Analysis of Kikuchi band contrast reversal in electron backscatter diffraction patterns of silicon, *Ultramicroscopy* 110 (3) (2010) 190–194. doi:10.1016/j.ultramic.2009.11.008.
- [110] R. Serneels, C. V. Roost, Q. Knuyt, Kikuchi patterns in transmission electron diffraction, *Philosophical Magazine A* 45 (4) (1982) 677–684. doi:10.1080/01418618208236197.
- [111] C. Van Roost, R. Serneels, Matrix methods for single and multiple inelastic scattering in electron diffraction, *Philosophical Magazine B* 56 (3) (1987) 397–409. doi:10.1080/13642818708221326.
- [112] J. Beauvillain, Diffusion des électrons par un cristal. introduction d'une notion de cohérence application aux diagrammes de lignes, *Physica Status Solidi (a)* 46 (2) (1978) 659–670. doi:10.1002/pssa.2210460231.
- [113] P. J. Beauvillain, Approche quantitative des contrastes en microscopie électronique, *Physica Status Solidi (a)* 66 (2) (1981) 675–682. doi:10.1002/pssa.2210660232.
- [114] G. P. Vdovynkin, The canyon diablo meteorite, *Space Science Reviews* 14 (6) (jul 1973). doi:10.1007/bf00224776.
- [115] R. Skála, I. Čisářová, M. Drábek, Inversion twinning in troilite, *American Mineralogist* 91 (5-6) (2006) 917–921. doi:10.2138/am.2006.1999.
- [116] T. Britton, J. Jiang, Y. Guo, A. Vilalta-Clemente, D. Wallis, L. Hansen, A. Winkelmann, A. Wilkinson, Tutorial: Crystal orientations and EBSD - Or which way is up?, *Materials Characterization* 117 (2016) 113–126. doi:10.1016/j.matchar.2016.04.008.
- [117] E. J. Kirkland, *Advanced Computing in Electron Microscopy*, Springer Science + Business Media, Berlin New-York, 2010. doi:10.1007/

978-1-4419-6533-2.

- [118] B. Pan, H. Xie, Z. Wang, Equivalence of digital image correlation criteria for pattern matching, *Applied Optics* 49 (28) (2010) 5501. doi:10.1364/ao.49.005501.
- [119] O. J. Woodford, Using normalized cross correlation in least squares optimizations, arXiv 1810.04320 (2018). arXiv:1810.04320v1.
- [120] A. Winkelmann, xcdskd: Tools and Methods for Kikuchi Diffraction (2018). doi:10.5281/zenodo.3689161. URL [https://xcdskd.readthedocs.io/en/latest/cross\\_correlation/cross\\_correlation\\_coefficient.html](https://xcdskd.readthedocs.io/en/latest/cross_correlation/cross_correlation_coefficient.html)
- [121] S. G. Johnson, The NLOpt nonlinear-optimization package (2020). URL <http://github.com/stevengj/nlopt>
- [122] T. B. Britton, C. Maurice, R. Fortunier, J. H. Driver, A. P. Day, G. Meaden, D. J. Dingley, K. Mingard, A. J. Wilkinson, Factors affecting the accuracy of high resolution electron backscatter diffraction when using simulated patterns., *Ultramicroscopy* 110 (12) (2010) 1443–53. doi:10.1016/j.ultramic.2010.08.001.
- [123] J. Alkorta, Limits of simulation based high resolution EBSD, *Ultramicroscopy* 131 (2013) 33–38. doi:10.1016/j.ultramic.2013.03.020.
- [124] E. Keil, E. Zeitler, W. Zinn, Zur Einfach- und Mehrfachstreuung geladener Teilchen, *Zeitschrift für Naturforschung A* 15 (12) (1960) 1031–1038. doi:10.1515/zna-1960-1202.
- [125] H. Zhong, Q. Shi, Z. Chen, C. Dan, S. Zhong, H. Wang, Residual-based pattern center calibration in high-resolution electron backscatter diffraction, *Micron* (2021) 103081doi:10.1016/j.micron.2021.103081.
- [126] C. Ernould, B. Beausir, J.-J. Fundenberger, V. Taupin, E. Bouzy, Integrated correction of optical distortions for global HR-EBSD techniques, *Ultramicroscopy* (2020) 113158doi:10.1016/j.ultramic.2020.113158.
- [127] J. M. Zuo, Automated lattice parameter measurement from HOLZ lines and their use for the measurement of oxygen content in  $\text{YBa}_2\text{Cu}_3\text{O}_{7-\delta}$  from nanometer-sized region, *Ultramicroscopy* 41 (1-3) (1992) 211–223. doi:10.1016/0304-3991(92)90110-6.
- [128] A. Morawiec, Formal conditions for unambiguous residual strain determination by CBED, *Philosophical Magazine* 85 (15) (2005) 1611–1623. doi:10.1080/09500830500041146.
- [129] J.-L. Rouviere, A. Béch , Y. Martin, T. Denneulin, D. Cooper, Improved strain precision with high spatial resolution using nanobeam precession electron diffraction, *Applied Physics Letters* 103 (24) (2013) 241913. doi:10.1063/1.4829154.
- [130] V. B. Ozdol, C. Gammer, X. G. Jin, P. Ercius, C. Ophus, J. Ciston, A. M. Minor, Strain mapping at nanometer resolution using advanced nano-beam electron diffraction, *Applied Physics Letters* 106 (25) (2015) 253107. doi:10.1063/1.4922994.
- [131] Y. Martin, J. L. Rouviere, J. M. Zuo, V. Favre-Nicolin, Towards a full retrieval of the deformation tensor F using convergent beam electron diffraction, *Ultramicroscopy* 160 (2016) 64–73. doi:10.1016/j.ultramic.2014.12.009.
- [132] G. Guzzinati, W. Ghielens, C. Mahr, A. B   , A. Rosenauer, T. Calders, J. Verbeeck, Electron Bessel beam diffraction for precise and accurate nanoscale strain mapping, *Applied Physics Letters* 114 (24) (2019) 243501. doi:10.1063/1.5096245.
- [133] C. Mahr, K. M  ller-Caspary, T. Grieb, F. F. Krause, M. Schowalter, A. Rosenauer, Accurate measurement of strain at interfaces in 4D-STEM: A comparison of various methods, *Ultramicroscopy* 221 (2021) 113196. doi:10.1016/j.ultramic.2020.113196.
- [134] K. Kaufmann, C. Zhu, A. S. Rosengarten, D. Maryanovsky, T. J. Harrington, E. Marin, K. S. Vecchio, Crystal symmetry determination in electron diffraction using machine learning, *Science* 367 (6477) (2020) 564–568. doi:10.1126/science.aay3062.
- [135] K. Kaufmann, C. Zhu, A. S. Rosengarten, K. S. Vecchio, Deep neural network enabled space group identification in EBSD, *Microscopy and Microanalysis* 26 (3) (2020) 447–457. doi:10.1017/s1431927620001506.
- [136] K. Z. Baba-Kishi, D. J. Dingley, Backscatter Kikuchi diffraction in the SEM for identification of crystallographic point groups, *Scanning* 11 (6) (1989) 305–312. doi:10.1002/sca.4950110605.
- [137] D. Van Dyck, Persistent misconceptions about incoherence in electron microscopy, *Ultramicroscopy* 111 (7) (2011) 894–900. doi:10.1016/j.ultramic.2011.01.007.